# A TRIDENT SCHOLAR PROJECT REPORT

NO. 486

**Numerical Simulation of Laser-Induced Drop Evaporation**

by

Midshipman 1/C Stefano Pineda, USN


UNITED STATES NAVAL ACADEMY
ANNAPOLIS, MARYLAND

This document has been approved for public release and sale; its distribution is unlimited.

USNA-1531

# REPORT DOCUMENTATION PAGE

*Form Approved*
*OMB No. 0704-0188*

Public reporting burden for this collection of information is estimated to average 1 hour per response, including the time for reviewing instructions, searching existing data sources, gathering and maintaining the data needed, and completing and reviewing this collection of information. Send comments regarding this burden estimate or any other aspect of this collection of information, including suggestions for reducing this burden to Department of Defense, Washington Headquarters Services, Directorate for Information Operations and Reports (0704-0188), 1215 Jefferson Davis Highway, Suite 1204, Arlington, VA 22202-4302. Respondents should be aware that notwithstanding any other provision of law, no person shall be subject to any penalty for failing to comply with a collection of information if it does not display a currently valid OMB control number. **PLEASE DO NOT RETURN YOUR FORM TO THE ABOVE ADDRESS.**

| **1. REPORT DATE** *(DD-MM-YYYY)* | **2. REPORT TYPE** | **3. DATES COVERED** *(From - To)* |
|---|---|---|
| 5-20-19 | | |

4. TITLE AND SUBTITLE
Numerical Simulation of Laser-Induced Drop Evaporation

**5a. CONTRACT NUMBER**

**5b. GRANT NUMBER**

**5c. PROGRAM ELEMENT NUMBER**

**6. AUTHOR(S)**
Pineda, Stefano

**5d. PROJECT NUMBER**

**5e. TASK NUMBER**

**5f. WORK UNIT NUMBER**

**7. PERFORMING ORGANIZATION NAME(S) AND ADDRESS(ES)**

**8. PERFORMING ORGANIZATION REPORT NUMBER**

**9. SPONSORING / MONITORING AGENCY NAME(S) AND ADDRESS(ES)**
U.S. Naval Academy
Annapolis, MD 21402

**10. SPONSOR/MONITOR'S ACRONYM(S)**

**11. SPONSOR/MONITOR'S REPORT NUMBER(S)**
Trident Scholar Report no. 486 (2019)

**12. DISTRIBUTION / AVAILABILITY STATEMENT**

This document has been approved for public release; its distribution is UNLIMITED.

**13. SUPPLEMENTARY NOTES**

**14. ABSTRACT**
Despite the rapid development of naval laser weapon systems, applications used to model High-Energy Lasers (HEL) in maritime environments are still incomplete. When a high-energy laser interacts with raindrops, fog, or other aqueous aerosols, the laser propagation and drop thermodynamics are coupled through the absorption-dependent vaporization process. Experiments with small droplets have shown that laser-droplet interactions may fall in two regimes – a "slow heating" regime where the drop rapidly evaporates due to elevated surface temperature, and a "fast heating" regime where the drop explosively breaks apart due to the pressure wave from spontaneous vaporization. Related numerical studies have ignored internal drop dynamics, assuming either spatially isothermal drops or assuming that heat transfer is by diffusion only. Recent experiments with larger laser-irradiated drops have shown that temperature fluctuations and internal drop dynamics are not negligible when drop diameter is on the order of 1 mm, e.g. in rain or sea spray. These experiments measured drop surface temperatures during a "slow heating" regime, but were unable to measure temperatures on the interior of the drop, where spontaneous vaporization is most likely to occur.
This research uses computer simulations to explore the laser heating, fluid dynamics, and evaporation of large water drops in order to determine internal drop temperatures and predict the onset of a "fast heating" regime. Simulations are run using COMSOL Multiphysics, a commercial solver based on the Finite Element Method. A geometric (ray) optics approach is used to generate internal volumetric heating distributions within a drop. This heating distribution is then applied to drops with different shapes and sizes, with increasing physical complexity to evaluate the effects each physical assumption has on the drop dynamics. The simulation is validated with experimental data on drop surface temperature, temperature variance, and vaporization rate, and is then extended to explore the effects of a range of parameters including laser irradiance and wavelength, drop shape, and external forcing. Dimensionless relationships between laser parameters and environmental conditions generated in this study can then be applied to laser propagation applications to enhance their predictive capabilities.

**15. SUBJECT TERMS**
Direct Numerical Simulation, Finite Element Method, Laser Propagation, Laser Heating, Computational Fluid Dynamics, COMSOL

| **16. SECURITY CLASSIFICATION OF:** | | | **17. LIMITATION OF ABSTRACT** | **18. NUMBER OF PAGES** | **19a. NAME OF RESPONSIBLE PERSON** |
|---|---|---|---|---|---|
| **a. REPORT** | **b. ABSTRACT** | **c. THIS PAGE** | | 84 | **19b. TELEPHONE NUMBER** *(include area code)* |

U.S.N.A. --- Trident Scholar project report; no. 486 (2019)

# NUMERICAL SIMULATION OF LASER-INDUCED DROP EVAPORATION

By

Midshipman 1/C Stefano Pineda
United States Naval Academy
Annapolis, Maryland

_____ _____
(signature) (date)

Certification of Adviser(s) Approval

Associate Professor Cody J. Brownell
Mechanical Engineering Department

_____ _____
(signature) (date)

Associate Professor Evelyn M. Lunasin
Mathematics Department

_____ _____
(signature) (date)

Permanent Military Professor CDR Stuart R. Blair
Mechanical Engineering Department

_____ _____
(signature) (date)

Acceptance for the Trident Scholar Committee

Professor Maria J. Schroeder
Associate Director of Midshipman Research

_____ _____
(signature) (date)

**Abstract**

Despite the rapid development of naval laser weapon systems, applications used to model High-Energy Lasers (HEL) in maritime environments are still incomplete. When a high-energy laser interacts with raindrops, fog, or other aqueous aerosols, the laser propagation and drop thermodynamics are coupled through the absorption-dependent vaporization process. Experiments with small droplets have shown that laser-droplet interactions may fall in two regimes – a "slow heating" regime where the drop rapidly evaporates due to elevated surface temperature, and a "fast heating" regime where the drop explosively breaks apart due to the pressure wave from spontaneous vaporization. Related numerical studies have ignored internal drop dynamics, assuming either spatially isothermal drops or assuming that heat transfer is by diffusion only. Recent experiments with larger laser-irradiated drops have shown that temperature fluctuations and internal drop dynamics are not negligible when drop diameter is on the order of 1 mm, e.g. in rain or sea spray. These experiments measured drop surface temperatures during a "slow heating" regime, but were unable to measure temperatures on the interior of the drop, where spontaneous vaporization is most likely to occur.

This research uses computer simulations to explore the laser heating, fluid dynamics, and evaporation of large water drops in order to determine internal drop temperatures and predict the onset of a "fast heating" regime. Simulations are run using COMSOL Multiphysics, a commercial solver based on the Finite Element Method. A geometric (ray) optics approach is used to generate internal volumetric heating distributions within a drop. This heating distribution is then applied to drops with different shapes and sizes, with increasing physical complexity to evaluate the effects each physical assumption has on the drop dynamics. The simulation is validated with experimental data on drop surface temperature, temperature variance, and vaporization rate, and is then extended to explore the effects of a range of parameters including laser irradiance and wavelength, drop shape, and external forcing. Dimensionless relationships between laser parameters and environmental conditions generated in this study can then be applied to laser propagation applications to enhance their predictive capabilities.

**Keywords**
“Direct Numerical Simulation”
“Finite Element Method”
“Laser Propagation”
“Laser Heating”
“Computational Fluid Dynamics”
“COMSOL”

**Acknowledgements**
This research was funded by the Office of Naval Research, The Joint Technology Office, and the United States Naval Academy Trident Program.

# Table of Contents

# Tables and Figures

# Introduction

In maritime environments, laser weapons systems and laser communications frequently interact with liquid water. This water may be in the form of small aqueous aerosols such as in clouds or fog, or large water drops from rain or sea spray. In the atmosphere, lasers are scattered by Raleigh scattering from air molecules, Raman scattering through backscatter from air, and Mie scattering with atmospheric aerosols [1]. All of these modes of laser scattering degrade and attenuate the laser beam as it propagates through the atmosphere. Through understanding of electromagnetic interactions with matter, lasers have been used to measure both water vapor concentrations up to 2 km altitudes and trace gas pollutants in the atmosphere [1, 2].

Several Naval applications of lasers, including weapons and power transmission, involve the use of high-energy beams that do not travel passively through their environment. Molecular absorption from a high-energy laser beam will not only attenuate the beam, but will also heat the transmission medium: air, aerosols, and water drops. A significant amount of prior research has examined laser heating of air and aerosols. Heating of the air results in thermal blooming, a phenomenon where the temperature-dependent index of refraction of the air within the beam path increases, causing the beam to flare and defocus [3, 4]. This phenomenon is highly dependent on the intensity of the laser, wavelength, path length, wind, and air composition [3, 4]. In order to model this phenomenon, and propagation through a variety of atmospheric conditions, MODTRAN, a radiation propagation-modelling program, was developed. MODTRAN can account for atmospheric particulates such as clouds, fog, and rain in addition to aerosols [5].

With small aqueous aerosols like those in clouds or fog, two predominant heating regimes exist. The fast heating regime exists when the heat rate is high enough and the drop exceeds the critical temperature for spontaneous phase change, which is 305°C for water in atmospheric air. If any part of the drop reaches this temperature, then the drop will spontaneously explode [6]. If however the drop does not reach this temperature and it does not explode, then the drop falls in the slow heating regime. In the slow heating regime, evaporative cooling from the droplet surface can keep the drop below the critical temperature (see Figure 1). The droplet will rapidly evaporate, but will not explode [6]. For a 1 μm drop and an irradiance of $10^9$ W/m$^2$ from a $CO_2$ laser, Davies and Brock [7] calculated evaporation times between $10^{-4}$ and $10^{-3}$ seconds.

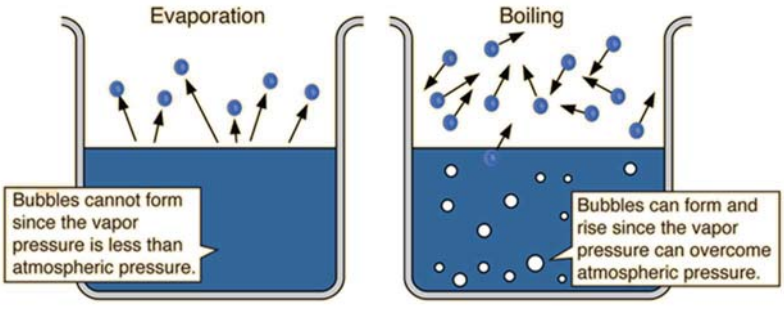


**Figure 1: Illustration of evaporation (left) occuring from surface at lower temperatures vs boiling vaporization (right) which begins at saturation temperature and may occur throughout the fluid [8]**

With large water drops, very little is known about their dynamics during radiative heating. An important contrast must be made between small aqueous aerosol “droplets”, with

diameters less than approximately 100 μm, and large water "drops", like rain, that may have a diameter of several millimeters. In both cases, the drop thermodynamics and the optical propagation of the laser are coupled through the absorption-dependent vaporization process. However, the large size of the drops results in fundamental changes to both the optical propagation and to thermo-fluid phenomena within the drop. Most important is the diminished role of the liquid's viscosity; in large drops the momentum forces within the fluid, driven by localized heating and buoyancy effects, will exceed the viscous forces. When this happens turbulent eddies will form within the drop, advection will dominate heat diffusion, and the drop temperature will vary rapidly both spatially and temporally. The net effect of this is that temperature in large drops is difficult to predict, and temperature-dependent processes like evaporation are similarly affected. The effects of laser radiation on the surface temperature of a large water drop are shown in Figure 2 [9]. This is all in contrast to small aqueous aerosols where convection within the droplet is assumed to be non-existent, liquid heat transfer is entirely conductive, and the droplet surface (and sometimes the entire droplet) is characterized using only a single temperature.

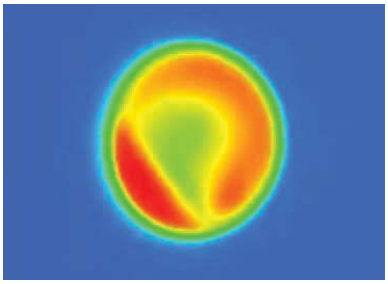

**Figure 2: Surface temperature of 2 mm drop irradiated by 600 W/m$^2$ laser [9]**

Recent work at the Naval Academy has measured evaporation rates on large, levitated, irradiated drops composed of both fresh and saline water [9]. An analytical model for absorption and evaporation rate that was previously used for small aerosols was extended and validated for use with large drops. Effects of drop size and irradiance were explicitly tested, and beam profile measurements were used to estimate off-axis attenuation through reflection and scattering. Evaporation rates were found to be consistent and predictable, despite potentially large fluctuations in surface temperature. The drop radius $R$ varies with time and depends on absorbed laser power, $\alpha I_o$, and enthalpy of vaporization per unit volume, $\rho h_{fg}$, as seen in (1). $\rho_D$ is the density of water.

$$R = R_o exp\left[-\left(\alpha I_o / 3\rho_D h_{fg}\right)t\right] \quad (1)$$

Subsequently, surface temperature measurements on irradiated, levitated drops using IR thermography have found that, after an initial transient heating period, a quasi-equilibrium process is supported [10]. During this process, the rate of energy absorption is balanced by the rate of evaporation. The mean drop surface temperature is set based on the required evaporation rate. As the drop evaporates and shrinks, the quasi-equilibrium temperature drops because the volume-dependent absorption rate decreases faster than the area-dependent evaporation rate [10].

One ultimate goal of this line of research is to provide physical models that can be incorporated into existing DoD high energy laser (HEL) codes such as HELTRAN (produced by

NRL) and HELEEOS (produced by AFIT) [11]. This will require an understanding of the effects of a number of variables that cannot readily be tested in an experiment. Even though all previous large-drop studies have been carried out with a slow evaporation regime, it is likely that an analogous high power regime exists where an HEL heats a water drop above its saturation temperature resulting in nucleate boiling.

Boiling inside drops occurs at 100°C as nucleation sites such as impurities and particulates facilitate boiling, but when they are not, greater temperatures are required to vaporize the drop. Within this large drop, there will be a dynamic temperature field that moves with internal convection. In the case where there are no nucleation sites, it is very important to determine the maximum temperature because this will dictate when the drop will reach its critical temperature and vaporize. Assuming that the drop is isothermal would require the average drop temperature to reach the critical temperature, which overestimates the time and energy to vaporize large drops. In real drops, the temperature at only one point in a dynamic velocity and temperature field needs to reach the critical temperature in order to vaporize and disperse the drop. Furthermore, raindrops interacting with an HEL may be in free-fall, and gravitational effects could be very different from what is seen with a single levitating drop. Varying these forces could greatly alter the natural convection within the drop thereby making the fluid dynamics within the drop either more or less important to determining the vaporization point.

Much research has been conducted on laser evaporation and vaporization of drops; however, they all make assumptions that this research will not. Some assumptions include no internal flow, no external forces, uniform heating, only explosive vaporization, no impurities, and stationary surface conditions [6, 7, 12, 13, 14, 15]. While these assumptions still generate useful results, the impact on the validity of the results when making these assumptions has not been determined. All of the referenced material assumes spherical drops or droplets. [7, 13, 14] all assume uniform heating of the drop. [13] and other sources ignored the varying concentrations of water in the surroundings; however many did not explicitly mention this assumption. Both [6, 7] assumed that there was no internal motion, and [14] assumed that the properties of water could be approximated with a volume average temperature.

It is difficult to determine the validity of these assumptions on such a small scale experimentally, so simulations will provide access to quantities that would be prohibitively difficult to measure. Simulations are capable of resolving detailed velocity and temperature profiles to help characterize the rate of mixing and the rate of vaporization. In addition to determining these rates, the maximum temperature and the greatest induced velocities can be determined for various combinations of drops and lasers. The effects of varying gravity, to simulate accelerating drops and free-fall, can also be explored in a systematic manner. Because some experimental data is available, the model can be partially validated with surface temperature data from [9]. Taken as a whole, the information drawn from a simulation such as the one proposed will result in an extension of our physical understanding of the laser drop problem.

# Background

Radiative heating of a water drop, and the resulting thermofluid and optical effects, presents a multi-physics problem that requires consideration of a number of coupled differential equations. This section presents a brief background on the most important equations that were solved using COMSOL as part of this research.

**Navier Stokes Equation (NSE):**

The NSE is used to model motion within fluids resulting from applied forces. NSE is an expression of Newton's second law of motion applied to fluids. A form of NSE is shown in (2) [16].

$$\rho(\partial_t \mathbf{u} + \mathbf{u} \cdot \nabla \mathbf{u}) = -\nabla p + \mu \nabla^2 \mathbf{u} + \boldsymbol{f} \tag{2}$$

In (2), $\partial_t \mathbf{u}$ is the local acceleration of the fluid and $\mathbf{u} \cdot \nabla \mathbf{u}$ is the convective acceleration of the fluid particle. $\mu \nabla^2 \mathbf{u}$ is the viscous force due to frictional resistance, and $\nabla p$ is the pressure gradient. $\boldsymbol{f}$ represents body forces acting on the fluid. One standard assumption that often accompanies NSE is the incompressibility condition shown in (3)

$$\nabla \cdot \mathbf{u} = 0 \tag{3}$$

Which implies that the divergence of the velocity field $\mathbf{u}$ is equal to zero. This means that the amount of fluid entering and exiting a fluid element is equivalent. To solve NSE with the incompressibility condition, the appropriate boundary and initial conditions need to be supplied. One may supply a no-slip boundary condition or periodic boundary condition. The initial condition is set as in (4)

$$\mathbf{u}(0, \mathbf{x}) = 0 \tag{4}$$

for fluid systems that begin at rest, for example. That is, the initial condition for the velocity field will be zero for all $\mathbf{x}$ at time t=0.

**Boussinesq Approximation:**

In Computational Fluid Dynamics (CFD), density is often fixed at a constant value in order to reduce computational cost. A constant density enables the simplification of complex problems. Despite assuming constant density, density differences are precisely how buoyancy driven forces are produced. Small density variations, when heat is applied, are responsible for imparting momentum within the drop that cannot be neglected. The Boussinesq approximation is a way to incorporate the momentum-effects of varying density while keeping density constant in conservation of mass and other terms. Equation (5) shows the basis of the Boussinesq approximation which is a temperature dependent variation of density [17].

$$(\rho_\infty - \rho) \approx \rho \beta (T - T_\infty) \tag{5}$$

In (5), $\rho$ is the local density, $\rho_\infty$ is the average surrounding density, and $\beta$ is the coefficient of thermal expansion. $T$ is the temperature at the location of interest while $T_\infty$ is the average surrounding temperature. This principle, (5), can then be substituted into the NSE to account for

buoyancy driven body forces acting on the fluid. The Boussinesq approximation incorporated into the NSE can be seen in (6) [16, 17].

$$\rho(\partial_t \mathbf{u} + \mathbf{u} \cdot \nabla \mathbf{u}) = -\nabla p + \mu \nabla^2 \mathbf{u} + \rho g \beta (T - T_\infty)\widehat{\boldsymbol{k}} \quad (6)$$

Here, the Navier Stokes equation has an added body force that is proportional to the temperature deviation from a reference average temperature. The gravitational acceleration vector is acting only in the $\widehat{\boldsymbol{k}}$ direction. This gravity vector will also vary in intensity based on whether the simulated drop is assumed to be in free fall, levitating, or accelerating.

While (6) accounts for the contribution of density driven flow into NSE, it does not track their temperature. The temperature of a differential fluid element will vary with the fluid flowing into the element, and the rate at which the fluid conducts heat to adjacent elements. This relationship is expressed in the Advection diffusion equation as (7) [18].

$$\frac{\partial T}{\partial t} = \alpha \nabla^2 T - \mathbf{u} \cdot \nabla T + Q_{abs} \quad (7)$$

In (7), $\frac{\partial T}{\partial \mathbf{t}}$, is the rate at which temperature is changing. $\alpha$ is the thermal diffusivity coefficient, and $\nabla^2 T$ and $\nabla T$ are the Laplacian and gradient of temperature respectively. $Q_{abs}$ is the heat absorption term representing the combined effect of the drop's absorptivity and the lasers irradiance. In order to solve (6) and (7), they must be supplied with appropriate boundary and initial conditions.

**Dimensionless Parameters**

In fluid flows, non-dimensionalization of the model equations can help bridge the behavior of flows that we see in laboratory experiments and the behavior of flows occurring in larger physical systems. This is due to the universality of turbulence. Essentially, the same characteristic turbulent behaviors can be observed in both a small air bubble and a large spherical container containing a liquid if the relevant dimensionless parameters are matched. A practical application of this information is that instead of measuring the drag force on a full sized ship, small scale laboratory experiments with matching dimensionless parameters can be used to calculate the forces that will be present at a larger scale [19]. Another relevant use of dimensionless parameters is in predicting heat transfer rates. Many experiments have been conducted to generate dimensionless equations with set ranges of validity. Using these equations within the relevant parameter ranges, heat transfer rates can be calculated for a wide array of set ups in fluids and solids. Some relevant dimensionless parameters are discussed below.

The Reynolds number is a number that is used to evaluate the ratio between inertial and viscous forces [18]. In many applications, it is used to determine the transition region between laminar and turbulent flow. Equation (8) shows how the Reynolds number can be calculated.

$$Re = \frac{uL}{\nu} \quad (8)$$

In (8), *Re* is the Reynolds number, *u* is velocity, *L* is a characteristic length, and *ν* is the kinematic viscosity of the fluid [19]. The Reynolds number is the most commonly used

dimensionless parameter, and it is very relevant in the simulation of fluids. Despite its relevance, the Reynolds number of the flow is usually difficult to define. The simulation creates this challenge because when simulating turbulence in a droplet, no free stream or characteristic velocity, *u*, can be defined. Because of this, other more relevant dimensionless parameters are defined. These include the Nusselt number, the Grashof number, the Bond number, and the Prandtl number.

The Nusselt number is relevant because it is the ratio between conduction heat transfer and convective heat transfer within a fluid [17]. The equation for the Nusselt number is (9).

$$Nu = \frac{hL}{k_f} \tag{9}$$

In (9), *Nu* is the Nusselt number, *h* is the convection coefficient, and $k_f$ is the thermal conductivity of the fluid being studied. Since the water drops in the simulation both conduct and convect heat internally, this dimensionless parameter helps explain the effect of changing the fluid, thus altering the thermal conductivity. It also shows the effect of the droplet shrinking, which changes the characteristic length or diameter of the droplet. Additionally, the Nusselt number also explains the behavior of the fluid air outside of the drop. There are both internal and external Nusselt numbers which describe the ratio of convective to conductive heat transfer.

The Grashof number is relevant in this simulation because it relates the buoyancy forces to the viscous forces in the fluid [17]. The equation for calculating the Grashof number can be seen in (10).

$$Gr = \frac{g\beta(\Delta T)}{\nu^2} L^3 \tag{10}$$

In (10), *Gr* is the Grashof number, $\Delta T$ is the difference between a surface temperature and a free stream temperature in natural convection applications. *L* is the characteristic length of a wall or surface in buoyancy driven flow. Typically, this dimensionless parameter is used to study air or water flowing past cooling fins; however, the temperatures are simply representative of a temperature gradient, which can be induced by a fluid boundary, or even laser induced heating.

The Rayleigh number is a similar dimensionless parameter shown in (11).

$$Ra = \frac{g\beta(\Delta T)}{\nu\alpha} L^3 \tag{11}$$

Since kinematic viscosity and thermal diffusivity, $\alpha$, have units of $m^2/s$, they are interchangeable in dimensionless equations. The Rayleigh number is also used to characterize buoyancy induced flow regimes [17].

The Bond number measures the ratio between buoyancy forces and surface tension. It is calculated using (12) [20].

$$Bo = \frac{\Delta\rho g L^2}{\sigma} \tag{12}$$

In (12), *Bo* is the Bond number, and $\sigma$ is surface tension. The Bond number is important when evaluating the surface behavior and shape when a droplet is immersed in a low-density phase, primarily gas [20]. A water drop in oil will behave very differently from a water drop in air; thus, the $\nabla\rho$ accounts for the density difference between the fluid drop and the density of the surrounding gas.

The Prandtl number describes the ratio between the viscous and thermal diffusion rate within a fluid. It can be calculated from (13) [17].

$$Pr = \frac{\nu}{\alpha} \tag{13}$$

In (13), $\nu$ is the kinematic viscosity while $\alpha$ is the thermal diffusivity of a fluid. This ratio helps quantify whether conduction or convection is the dominant method of heat transfer within a fluid. For relatively large Prandtl numbers, viscous effects will dominate and convection will affect a larger role in the heat transfer. Conversely, very small Prandtl numbers are indicative of fluids that tend to conduct more than they convect.

With simulations resolved in COMSOL an extension to this research could incorporate, dimensionless parameters in data reduction in order to generate dimensionless equations that describe the effects of lasers on drops. Generating dimensionless equations that relate the intensity of the laser, the size of the drop, and other fluid properties is of interest to this investigation because it will allow the results to apply to a wider array of laser drop combinations. To incorporate results from this research into HEL simulation applications such as HELCAP and HELEEOS, the results need to be nondimensionalized. By generating nondimensionalized equations, the significance of the results will go from a few laser drop combinations, to an entire spectrum of potential laser drop combinations. The Reynolds number, the Nusselt number, the Grashof number, the Bond number, and the Prandtl number are just a few of the dimensionless parameters that may be included in the dimensionless equations that may be generated. These dimensionless equations could be constructed to help approximate evaporation half-lives, maximum drop temperature, and rate of mixing for a variety of laser drop combinations. Before running simulations, however, dimensionless parameters will also aid in the understanding of the internal drop dynamics. This understanding could help predict relevant scales that correlate with the necessary resolution to run a DNS.

As heat mixing begins, large eddies form at a scale proportional to the whole drop in the energy containing range [21]. These larger eddies are non-uniform and drive the formation of smaller eddies. Below a certain dimensionless characteristic length $l_{EI}$ eddies become isotropic or uniform throughout a fluid. Because there is a small size difference between the largest and smallest eddies in this drop simulation, the turbulence is far from isotropic. Despite the lack of isotropy, larger sized eddies still break up into smaller eddies until the viscous forces of the fluid can dampen the smallest eddies. The smallest sized eddies that can exist in a fluid are described by Kolmogorov scales for length, velocity, and time. Energy cascades down, from larger to smaller eddies, until it is dissipated by viscous forces at the Kolmogorov scale [21].

The Kolmogorov length scale can be determined using (14).

$$\eta = \left(\frac{\nu^3}{\varepsilon}\right)^{1/4} \tag{14}$$

In (14), $\eta$ is the Kolmogorov length scale, and $\varepsilon$ is a characteristic dissipation rate. This equation shows that with more viscous fluids, the largest eddies will be smaller than in fluids with lower viscosities. There are also similar equations to calculate the Kolmogorov timescale and Kolmogorov velocity scale, but these are less imperative in determining the smallest reasonable resolution size. To resolve an eddy only a few points within the eddy are necessary to determine the local vorticity, therefore resolving the flow to a finer grid will waste computational time.

While the Kolmogorov scale is the smallest scale for turbulent motion, there is still scalar dissipation that may occurs at smaller scales depending on the Prandtl number. The Batchelor scale applies to the micro mixing of scalar quantities such as concentrations of impurities and temperatures [22]. The Batchelor length scale is similar to the Kolmogorov scale and can be calculated from (15) [22].

$$\lambda_B = \left(\frac{\nu D^2}{\varepsilon}\right)^{1/4} \tag{15}$$

In (15), $\lambda_B$ is the Batchelor length scale and $D$ is the molecular or thermal diffusivity. The Batchelor scale describes what amount of diffusion will occur in a Kolmogorov time scale. This time scale represent how long it takes the smallest eddies to dissipate.

**Laser Propagation and Absorption**

When a droplet is exposed to laser irradiation, two major heating regimes exist. The explosive vaporization regime occurs when the vaporization temperature of the fluid droplet is exceeded and the fluid quickly disperses into smaller droplets while the slow evaporation regime occurs when this explosive process does not occur [7]. The latter slow evaporation regime is the subject of this research. In this regime, the droplet evaporates relatively slowly. This evaporation is accelerated by the laser energy absorption within the drop. As the drop evaporates, it decreases in size and changes the dynamics within the drop.

Before looking inside the drop, a basic picture of laser refraction through a droplet is beneficial. As the laser hits the surface of the droplet, because it is entering a medium with a different refractive index or optical density, its path will be refracted [23]. When the second material has a greater refractive index, the incident light will refract closer to the normal of the surface as it passes through. This phenomenon can be observed in Figure 3 where a laser incident on a droplet is refracted toward the normal vector upon entry into the droplet, and away from the normal as the rays exits the drop [2]. The amount of refraction observed in this phenomenon can be calculated using Snell's law for refraction.

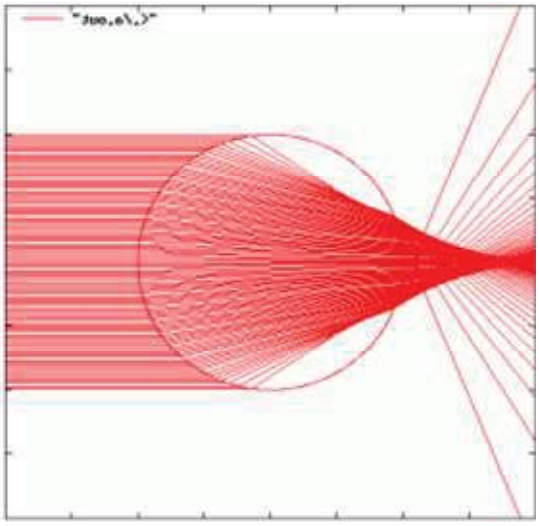

**Figure 3: Laser refraction through a sessile drop [2]**

It is important to note that this drop is not drawn to scale with this simulation. It does however highlight the fact that there is not uniform heating throughout the drop.

This non-uniform heating is modelled using the Beer-Lambert Law. Beer-Lambert is used to calculate the absorptivity of a sample and determine how much of the incident irradiation is absorbed, transmitted, and reflected. At both the entering and exiting interfaces, a fraction of the radiation reflects off the surface. As the laser passes through a drop, a fraction *f* is reflected on the on the outside, away from the droplet, and a fraction *m* is reflected back into the drop at the exiting boundary. These fractions will vary with the refractive index of the fluid as well as the incident angle to the fluid's surface. Using *f* and *m*, the amount of radiation passing through a fluid, assuming no absorption, can be calculated with (16) [24].

$$P_0 = P'(1-f)(1-m) \tag{16}$$

In (16), $P_0$ is the amount of radiation passing through both interfaces and *P'* is the incident radiation. Both of these radiation terms contain units of power because they are a flux of energy through the drop.

Since all real fluids reflect and absorb incident radiation, the absorption must also be characterized. The absorption of a fluid with a given path length *b* is described by a linear form of the Beer Lambert law (17) [24].

$$A = -\log_{10}\frac{P}{P_0} = abc \tag{17}$$

In (17), *A* is the absorption of the fluid, *P* is the amount of radiation passing through the fluid species, *a* is the absorbance of the fluid, and *c* is the concentration of the absorbing species in the fluid. (16) and (17) describe the macroscopic behaviors of the laser interactions with many simplifying assumptions. While this expression of the Beer-Lambert law, (15), is useful for macroscopic behaviors, the differential form in (18) describes how the laser will behave as it propagates through a fluid [25].

$$\frac{\partial I}{\partial z} = \alpha(T, \lambda) I \tag{18}$$

In (18), $\frac{\partial I}{\partial z}$ is the rate at which the intensity of the laser changes with respect to the distance it has travelled through the fluid. Intensity is power over a given angle. $\alpha(T)$ is the temperature dependent absorption of the fluid, and $I$ is the laser intensity [25].

**Finite Element Method**

Equations that govern fluid transport, heat transfer, and physics in general can be expressed as a system of differential equations. In general, the system of equations can be solved analytically only for sample cases. For more complex cases we can approximate the solution numerically. For fluids simulation problems, the Finite Element Method (FEM) serves this purpose well.

To employ the FEM, first the physical system being modeled is described in terms of partial differential equations. While these equations describe the mathematics and physics governing the motion of energy and momentum, they still ignore effects on a molecular level. This is precisely why the governing differential equations only model the physical system instead of fully describing it [27].

When the governing equations, initial conditions, and boundary conditions have been established, the strong form for a model has been fully defined. The strong formulation involves the evaluation of high order derivatives that can be relaxed by transforming the equation into its weak formulation or variational formulation [27]. The weak formulation is obtained by multiplying the PDE by a test function and then integrating over the spatial domain. The resulting equation is required to hold for all test functions from a collection of functions having certain properties. Hence, the equations are required to hold in the sense of distribution, instead of pointwise. Once the weak formulation is obtained, procedures for the standard Galerkin finite element method can be emplyed [27].

**Methods: Sequential Simulation Process**

COMSOL is a multi-physics simulation software that allows for the integration of a number of physical principles into one simulation. Because this software has so many layers, this research employs a sequential formulation to develop a final model. The model is broken into various goals that can be compiled and assessed as intermediate steps towards construction of the final model. The original goal was to run a DNS, but no DNS simulations were conducted. A DNS implies that all levels of fluid motion, from the largest to the smallest turbulent eddies, are resolved [25]. Conducting a DNS is often prohibitively expensive in terms of computational time, but because the smallest eddies observed experimentally in Tracey and Brownell's work [8,9], were not substantially small compared with the simulation volume, a DNS was originally pursued. Since a DNS proved too taxing, under-resolved laminar flow simulations were used to reduce the computational cost. Under-resolved simulations do not calculate energy dissipation or motion smaller than the smallest grid elements used to discretize the FEM drop. Some simulations with smaller drops may have in fact captured the smallest scales of motion, but

further mesh refinements were not evaluated to determine if breakup beyond the smallest observed scales would occur.

A flow chart of the completed milestones to develop the simulation is shown in Figure 4. The boxes in blue represent existing COMSOL simulations that demonstrate the use of the specific modules and boundary conditions that are employed while the orange boxes show the type of simulation resolved using the different modules.

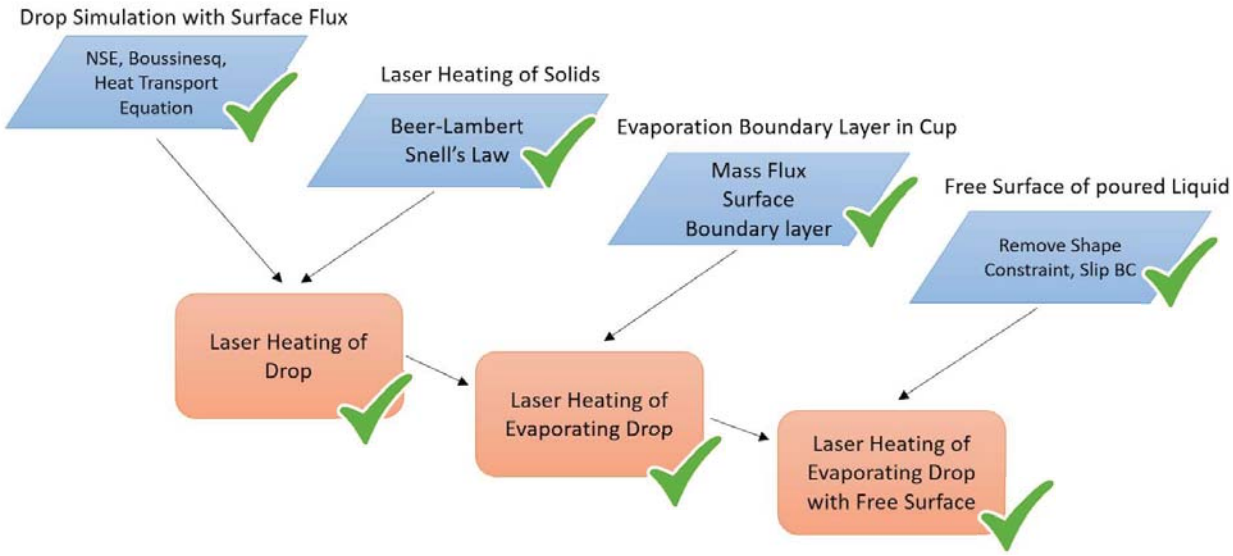


**Figure 4: Flowchart of simulation development**

For the first simulations, there was no evaporation or laser heating. Instead, a more simple constant surface heat flux was applied to heat the drop. This artificial surface heating drove convection within the drop.

After simulating a constant surface flux, laser heating of solids was also simulated. When a laser irradiates a semitransparent material, the beam is partially reflected, absorbed, and transmitted. The temperatures in a piece of absorbing glass can be modelled using the Heat transfer diffusion equation (7) with a velocity field that is zero everywhere. With the convective term eliminated, this becomes a conduction equation.

After developing all the components of this multi-physics problem, the sequential process of improving the drop simulation began. First, the laser heating replaced the surface flux heating on the drop. After the drop responded to the laser heating, the evaporative cooling was modelled with a moving mesh and convection. The drop will still be assumed spherical and it delivered results. The spherical assumption should be validated because larger drops tend to deform from the ideal spherical shape. The free surface condition was not included, but it would make a good extension to the model to generate more realistic results.

Most transient effects were captured in all iterations of the model, but the effects of a moving boundary and water drop deformation were not incorporated until after most other

objectives had been met. This approach assumes that the thermodynamic effects of evaporation (the lost latent heat) are much more important than the kinetic effects (the change in drop size).

Transient heat transfer phenomena within the drop and between the drop and its surroundings, including the initial heating of the water, transport of temperature throughout the drop, and latent heat transfer to the surroundings, were captured by solving the equations as proposed in both space and time and with suitable boundary conditions. Both the convection and mass transfer coefficients were obtained from the literature, but their accuracy can also be assessed via comparison of surface temperature with experimental results.

A simulation with this level of fidelity, that does not yet capture the moving drop boundary, was used to determine peak drop temperature, internal motion, vorticity, time to boiling, and an appropriate architecture for extracting data.

During the development of the full simulation, parameters were varied to reduce the computational cost. The computational cost increases with the Reynolds number, decreasing grid size, and the desired accuracy of the simulation [25]. In order to reduce the computational cost throughout the research, reduced droplet sizes, and reduced grid refinement were employed; however, all of these reduce the accuracy of the dynamics that will be observed within the drop. The simulations were all conducted on The Naval Academy's Sedna Server. It is a 144 GB RAM server with 12 cores at 2.53 GHz. This server will be utilized for all future simulations and the entire test matrix. The values that will be applied to the simulation through the test matrix are listed in Table 1.

**Table 1: Test matrix for fully functional model**

| Varied Parameter | Fluid | Diameter | Intensity | Wavelength |
|---|---|---|---|---|
| **1. Validation** | Water | 1.4 mm | 1000 W/cm2 | 1064 nm |
| **2. Size** | Water | 100 µm<br>1 mm<br>5 mm | 500 W/cm2 | 1064 nm |
| **3. Intensity** | Water | 1 mm | 500 W/cm2<br>5 kW/cm2<br>50 kW/cm2 | 1064 nm |
| **4. Wavelength** | Water | 1 mm | 500 W/cm2 | 532 nm<br>1064 nm<br>10 µm |
| **5. Viscosity** | 1/2x µ water<br>1x µ water<br>2x µ water<br>16x µ water | 1 mm | 500 W/cm2 | 1064 nm |

In the validation section of the test matrix, the conditions from Brownell's previous experimentation [9] were simulated in order to validate the model. In order to validate the model, various irradiances, convection coefficients, and internal drop forcing were tested. The most accurate combination of parameters was then set as the validation model to compare against experimental data from [9]. Accuracy of the parameters was determined by comparing the maximum and average surface temperatures with date from experiments conducted in [9]. After validating this model, it was used as a backbone from which to extrapolate and extend simulation parameters in order to understand laser-drop behaviors that were not physically experimented. This extrapolation provides insight into the behavior of HEL irradiated drops. The final simulation varied a coefficient on the polynomial that describes the temperature dependent viscosity of water within non-isothermal flow simulations in COMSOL.

# Background for Simulations

**Rayleigh Numbers and Expected Motion**

In order to predict expected motion within a laser heated drop, expected Rayleigh numbers were computed using the formula in (11). Using a characteristic length for a 1cm drop, a 10cm drop, and the Free Convection COMSOL model (described in Appendix A), Rayleigh numbers were computed for various average temperatures as shown in Table 2. The *Free Convection Tutorial* [28] was used for comparison because the flow regime is known. By knowing the Rayleigh number and the characteristic motion within the free convection model, flow regimes are estimated for drop simulations based on anticipated Rayleigh numbers.

The thermal expansion coefficient, the kinematic viscosity, and the thermal diffusivity of water ($\beta$, $v$, and $\alpha$ respectively) were interpolated from [29] for various average water temperatures.

| Average Temperature (°C) | $\beta$ | $v$ | $\alpha$ |
|---|---|---|---|
| 15 | 0.000147 | 1.14E-06 | 1.40E-07 |
| 60 | 0.000522 | 4.74E-07 | 1.55E-07 |
| 90 | 0.000695 | 3.25E-07 | 1.66E-07 |

| Parameters | | Rayleigh Number at Varied Temperatures |
|---|---|---|
| Drop: 1 cm diameter | | 3.6 E+05 |
| ΔT (°C) | 40 | 2.8 E+06 |
| Characteristic Length (m) | 0.01 | 5.1 E+06 |
| Convection cup | | 1.2 E+07 |
| ΔT (°C) | 20 | 8.9 E+07 |
| Characteristic Length (m) | 0.04 | 1.6 E+08 |
| Drop: 10 cm diameter | | 6.3 E+07 |
| ΔT (°C) | 7 | 4.9 E+08 |
| Characteristic Length (m) | 0.1 | 8.8 E+08 |

**Table 2: Predicted Rayleigh numbers evaluated at varying average temperatures for 1 cm drop, 10 cm drop, and COMSOL convection cup tutorial**

Calculated values in Table 2 show that both drop scenarios will be within two orders of magnitude for Rayleigh number. The flow regime within the convection cup is laminar. The convection cup is a tutorial that was used to start building the drop models and to compare the motion within. Laminar flow in the cup is in agreement with the transition Rayleigh number for vertical flat plates of $10^9$ [30]. Below Rayleigh numbers of about two thousand, heat transfer is due entirely to conduction [30]. Since the drop Rayleigh numbers are between these regime-transition values, laminar flow is expected to develop in both drop sizes.

# Overview of Simulations

To develop a model that accounts for most of the relevant physics, models incorporating fewer physical considerations were first simulated. A flowchart depicting the simulation development is shown in Figure 5.

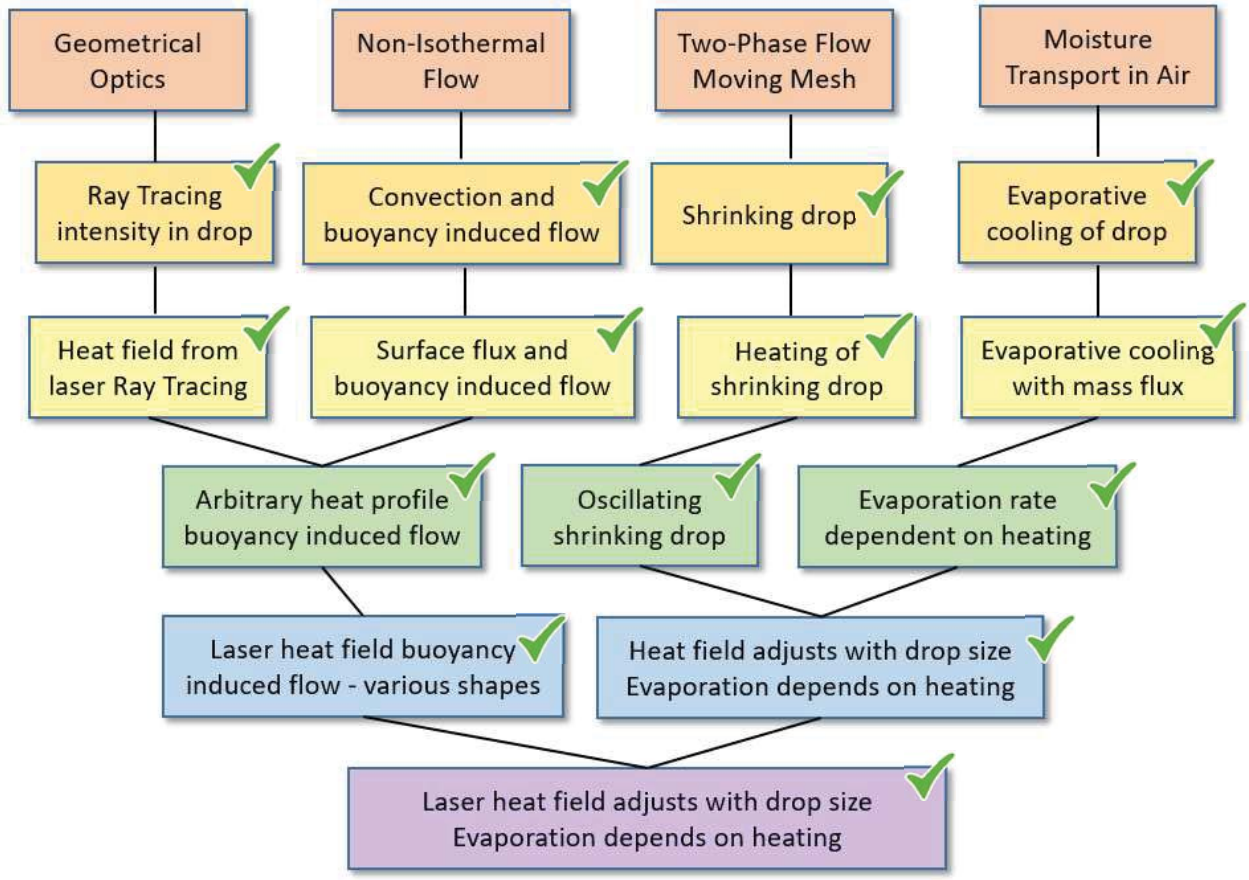


**Figure 5: Flowchart of simulation development**

Geometrical Optics were used to track rays as they reflect, refract, and dissipate in a water drop. Initially, simulations only tracked the intensity of the rays as they propagated through the drop, but by defining an imaginary index of refraction for water, COMSOL calculated the power deposited throughout the absorbing medium. This deposited power was then extracted to be used as a heat fields for the non-isothermal flow simulations.

Non-Isothermal Flow (NITF) links laminar flow with heat transfer in fluids. Either COMSOL employs the Boussinesq approximation, or it treats fluids as compressible to track variable density. First, simulations heated drops exclusively through uniform convection. After resolving convective heating, active heating of drops was simulated by employing surface heat fluxes. These simulations were conducted in two dimensions prior to expanding them to three dimensions due to increased computational times.

With resolved heat fields and sample slice profiles, an equation for an arbitrary heating function was developed in order to explore laser heating drop dynamics in axisymmetric drop simulations. Ray heating fields cannot be used in two-dimensional simulations, so a heating function enabled other two-dimensional studies such as heating of shrinking drops. After resolving heating from an arbitrary heating profile, three-dimensional simulations of drops heated by laser heat fields were resolved. First, a spherical drop with laser heating was simulated. Then, convection was added and the shape of the drop was varied to generate more varied fluid dynamics. In addition to the varied shapes, body forcing functions were also introduced to simulate acoustic levitation or a drop in freefall.

Using the Two-Phase Flow Moving Mesh module, simulations to track shrinking drops were developed. The first two-dimensional axisymmetric simulations only considered a shrinking sphere with fluid dynamics or heat transfer inside or outside of the drop. After resolving a shrinking drop, a singular moving mesh tracking just the drop was utilized to study an axisymmetric shrinking drop with an arbitrary heating profile. A moving mesh also enables the tracking of free surfaces, so the free surface of an isothermal drop was tracked as it shrank, oscillated, and moved through air due to an applied body forcing function.

COMSOL's Moisture Transport in Air module can track moisture as it evaporates from a "wet surface" and moves through the air according to advection and diffusion. An axisymmetric evaporating drop was simulated as air flowed upward around the drop

In order to conduct these simulations, COMSOL tutorial were consulted. The COMSOL tutorials utilized are listed in the Appendices. Free Convection in a Water Glass helped resolve NITF. It is discussed in Appendix A [28]. The Luneburg lens heled resolve geometrical optics and it is discussed in Appendix B [31]. Modeling Laser Beam Absorption in Silica Glass with Beer-Lambert Law helped develop laser heating in solids, and it provided insights regarding how to handle laser-irradiated fluids [32]. It is discussed in Appendix C. Evaporative Cooling of Water was also consulted to determine appropriate boundary conditions and settings to resolve moisture transport in air [33]. This evaporative cooling tutorial is discussed in Appendix D.

The flowchart in Figure 5 is not exhaustive, as it does not enumerate all the simulations that have been conducted in this study. Not all simulations are discussed at length in this report. Simulations without check marks have yet to be constructed and resolved.

# Geometric Optics

**Ray Trace Intensity and Heat Source**

Using the Geometrical Optics physics interface in COMSOL, laser rays were irradiated upon a water drop. Using differential formulations of Fresnel's equations, Snell's law, and the Beer-Lambert law, both the intensity and the deposited power throughout the drop domain were resolved.

The first Ray Tracing simulations were modelled after the Luneburg lens tutorial in Appendix B [31]. The number of rays, the ray termination length, the diameter of the sphere, and the refractive index were all modified to simulate an irradiated water drop. Figure 7 shows the log of ray intensity for 100 tracked rays with an incident irradiance of 1000 W/m$^2$.

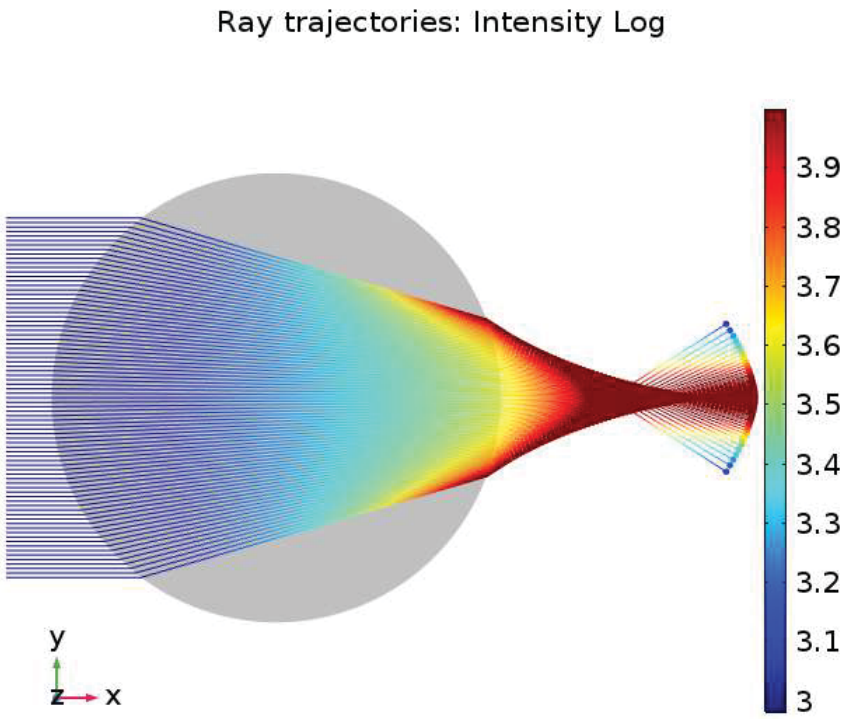


**Figure 6: Logarithm of ray intensity for 1cm diameter drop**

The logarithm of ray intensity is plotted in Figure 6. Very high intensity at the focal points makes the intensity everywhere else negligible by comparison; hence, the log of intensity is plotted. - This simulation irradiated 100 rays stacked vertically towards a three-dimensional drop. Here, the exiting rays appear to bend, however, the top and bottom rays bend the most, and other more central rays continue closer to horizontal which creates the illusion of bending rays. Because the rays in this simulation were not distributed spatially, another simulation was needed to generate a three-dimensional heating source.

To generate this heat source, a 1cm by 1cm grid released rays towards a 1cm diameter drop. The resulting heat source profiles are shown in Figure 7.

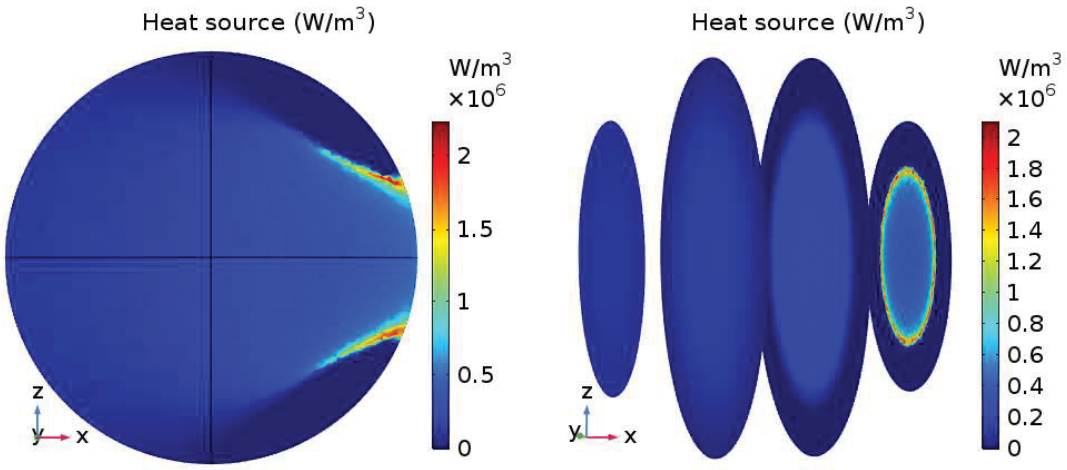


**Figure 7: Heating profiles from deposited ray power in absorbing media**

In Figure 7, the rays enter the drop from the left travelling in the positive X direction. The focusing from the drop highlights the concentrated heating of spherical laser-irradiated drops. This focused heating leads to very high temperature gradients when higher irradiances are employed. In an effort to generate similar heating profiles from the governing physics equations, the intensity data from Figure 7was plotted in Figure 8 for comparison.

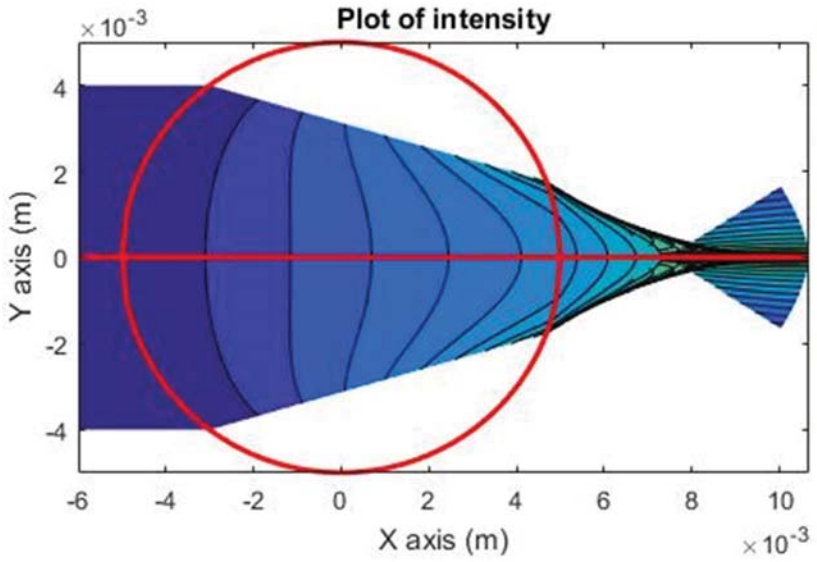


**Figure 8: Intensity plot of COMSOL data in MATLAB**

## MATLAB Validation of COMSOL Results

Using Snell's law and the Beer-Lambert law, a MATLAB code was developed to compute relative irradiance magnitudes throughout a drop profile. The code employed generated irradiance contours similar to those in COMSOL and it is included in Appendix E. This

agreement validates that both the COMSOL ray tracing, and the MATLAB computation accurately quantify the ray focusing of an irradiated drop. The MATLAB code did not account for Fresnel's law, and it assumes that the intensity of each ray does not decrease as it propagates through the drop. This leads to more heating throughout the drop. Figure 9 shows the set up for the MATLAB simulation.

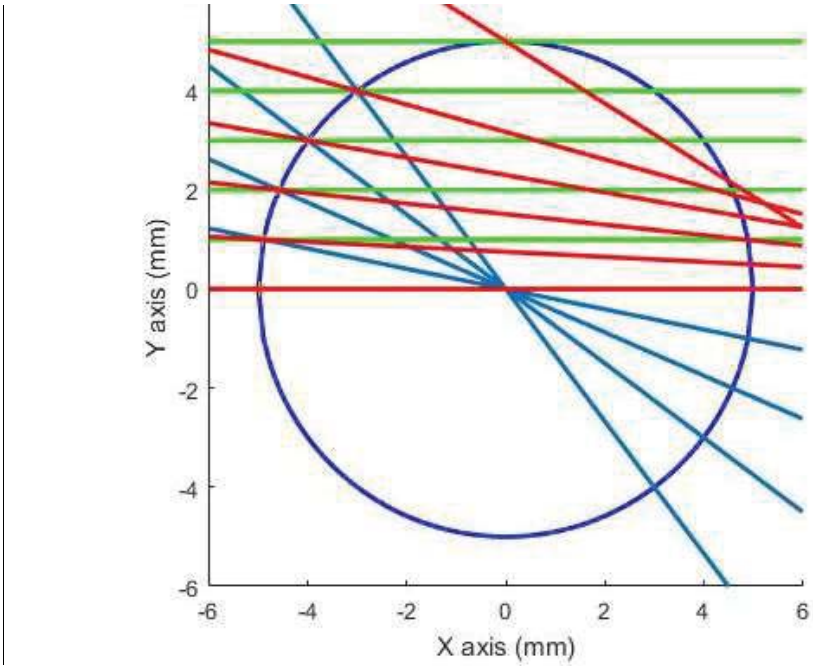


**Figure 9: Normal lines, incident rays, and refracted rays in a 1cm diameter circle**

In Figure 9, the green rays represent evenly spaced incident rays that irradiate the spherical drop. The blue lines are vectors normal to the surface of the drop where each incident ray enters the drop, and the red rays are refracted rays that propagate through the drop at a new angle. Using these geometrical and optical properties, the refracted rays were utilized to model intensity as shown in Figure 10.

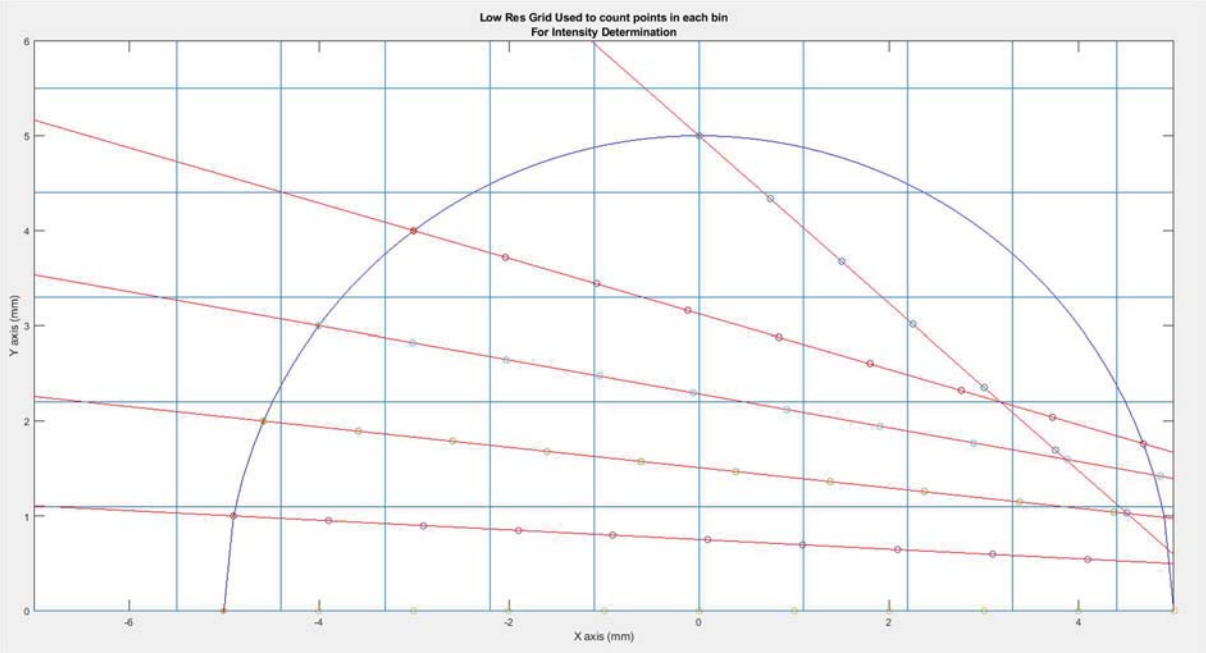


**Figure 10: Intensity map within irradiated drop**

To simulate intensity using Snell's law and the Beer-Lambert law, points were plotted along the refracted rays a set distance "*ds"*: determined by dividing the diameter of the drop by the number of points desired on each ray. With the coordinates of these points known, they were grouped into bins as depicted by the blue lines in Figure 10. To refine the contour of the laser intensity, 500 incident rays were included, 1000 points were plotted along each ray, and 100 bins and 50 bins were set in the x and y directions respectively. A plot of the points within the drop is shown in Figure 11.

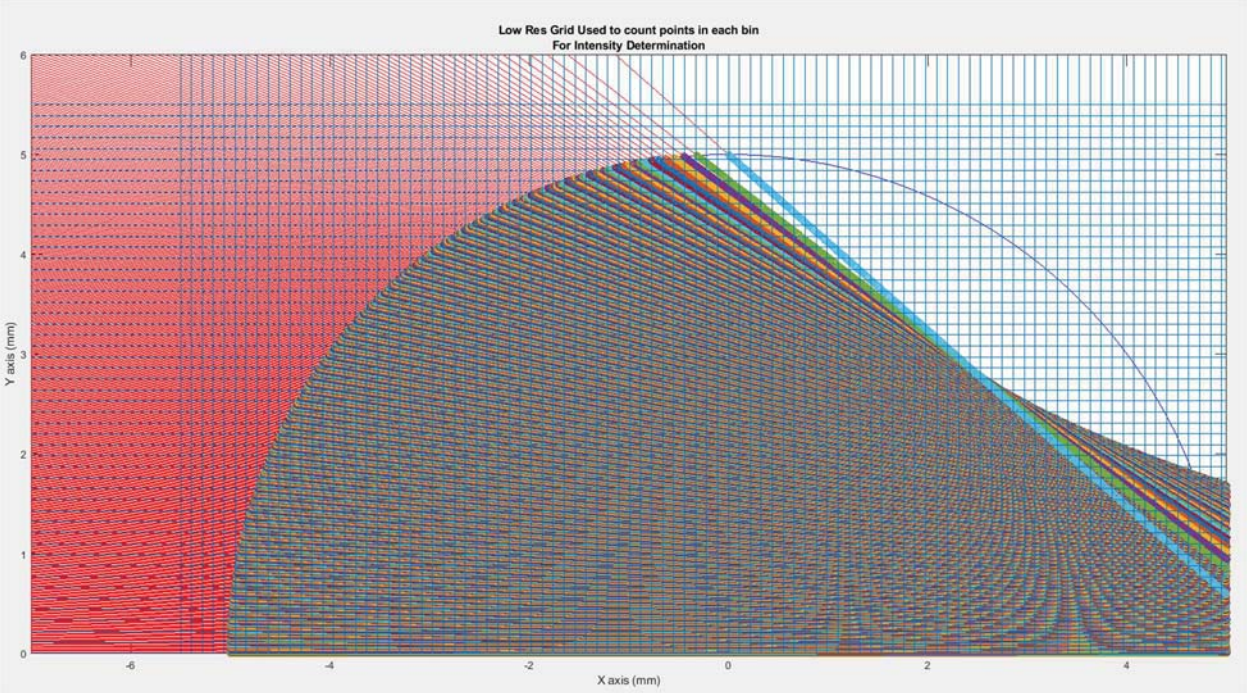


**Figure 11: Intensity dots with 500 rays, 1000 points per ray, 100 x bins, and 50 y bins**

To show the intensity contour generated by these equidistant points, a contour plot of the data was generated and is shown in Figure 12.

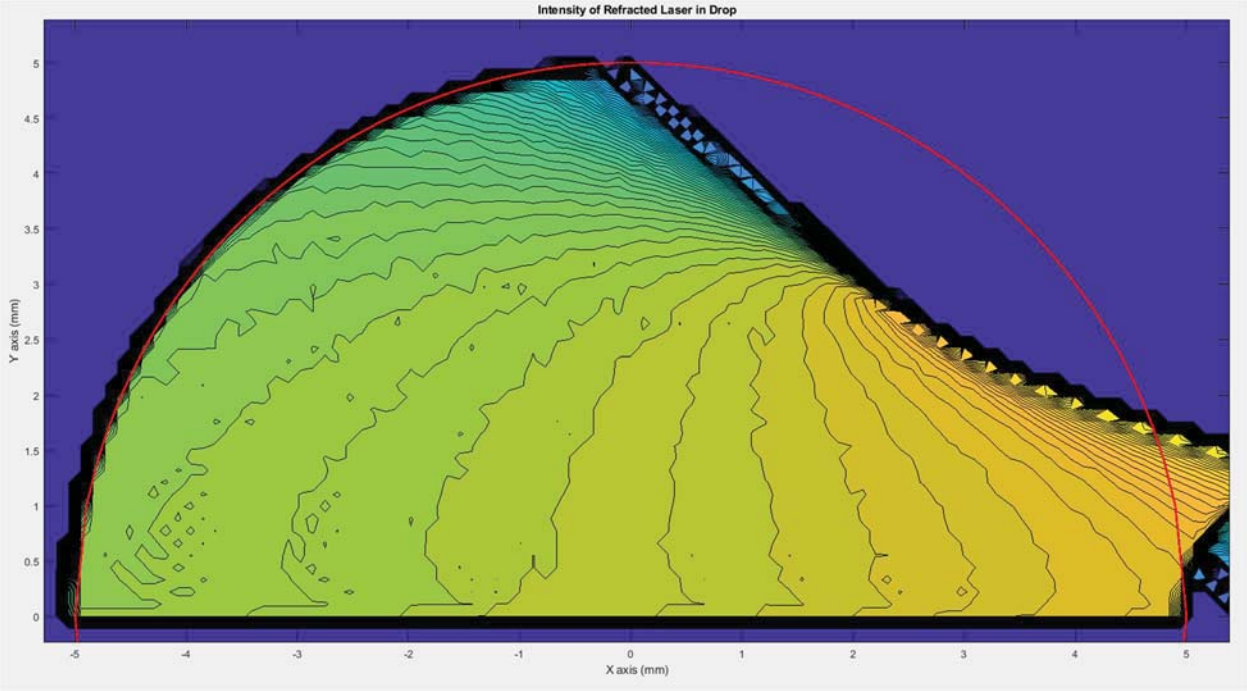


**Figure 12: Contour of irradiated drop with 500 rays, 1000 points per ray, 100 x bins, and 50 y bins**

In order to generate a smoother intensity profile, the number of rays, points and bins were all increased by a factor of ten, and the resulting contour plot is depicted in Figure 13.

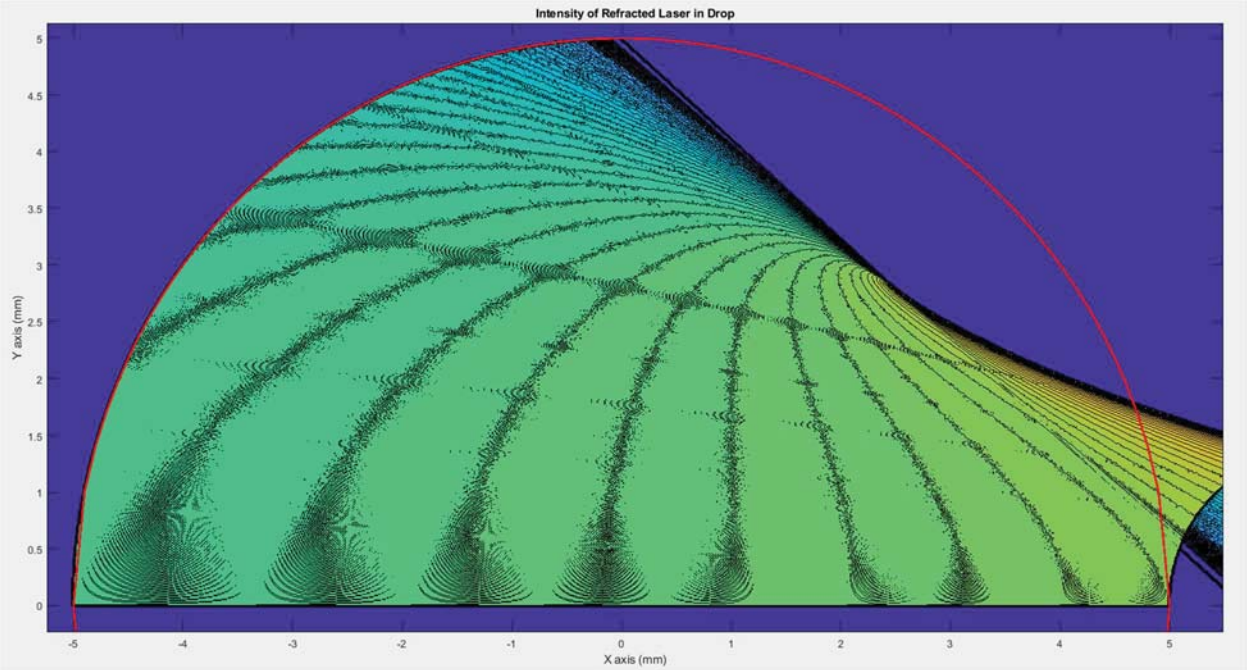


**Figure 13: Contour plot of irradiated drop with 5,000 rays, 10,000 points per ray, 1,000 x bins, and 500 y bins**

This simulation with 500,000 bins suffers from oversampling and shows shaded regions instead of distinct contours; however, qualitatively, it shows contours similar to the profile generated in COMSOL and graphed using MATLAB in Figure 8. This agreement validates that both the COMSOL Ray Tracing approach and the MATLAB first principles approach can accurately model laser heating intensity throughout an irradiated drop.

# Two-Dimensional Non-Isothermal Flow

**2D Axisymmetric Uniform Surface Flux**

In this simulation, a spherical axisymmetric drop was heated with a constant surface flux and both the Laminar Flow and Heat Transfer in Fluids physics interfaces were coupled through the Non-Isothermal Flow multiphysics coupling to resolve internal drop temperatures and motion. As the heat flux entered the drop, buoyancy driven flow motion concentrated the hotter water towards the top of the drop as would be expected.

The Free convection in glass of water tutorial, explained in Appendix A, was used as a model for this simulation. The parameters listed in Table 3 were utilized as inputs and setting in COMSOL. Instead of resolving a full three dimensional temperature and velocity field, only a slice of the axisymmetric solution needed to be resolved. This approach greatly increases performance at the cost of a dimension. Select result profiles from the simulation are shown in Figure 14.

**Table 3: Two-dimensional axisymmetric uniform surface flux parameters**

| Parameter | Value |
|---|---|
| Dimensions | 2D Axisymmetric |
| Diameter | 10 cm |
| Initial Drop Temperature | 5℃ |
| Uniform Heat Flux | 500 W/m$^2$ |
| Mesh | Fine |
| DOF | 16,816 (plus 121 internal DOFs) |
| Simulation time | 2 minutes |
| Solution time | 3 minutes 1 seconds |
| Time Steps | 459 |

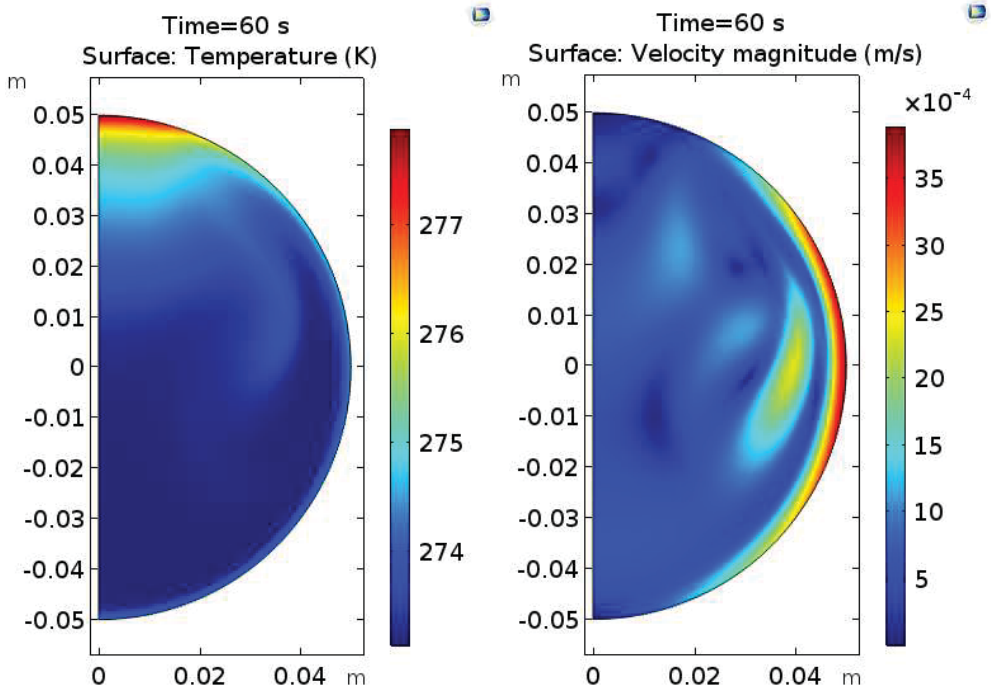


**Figure 14: Temperature and velocity profiles for uniform surface flux drop**

This simulation utilized 2D axisymmetric dimensions because it reduces the computational cost by taking advantage of geometrical symmetry in the problem. This axisymmetric simulation had temperature differences below 10℃ with velocities never exceeding 0.4 cm/s. Laser heating was oversimplified to prove methods that would generated expected motion. By generating predicted motion and heat transfer, the methods from this simulation could be extrapolated to simulations that are more realistic.

**Arbitrary Continuous Heating**

An arbitrary continuous heating profile that qualitatively resembles the heating profiles from ray tracing simulations was developed. This heating profile was developed in MATLAB through an iterative process in approximate the heating of a laser irradiated drop. This profile was used in many comparisons between different COMSOL settings in order to resolve future models faster and with greater fidelity. The scalable heating function is shown in (20) and a sample laser profiles is shown in Figure 15.

$$\dot{Q} = k(z + 0.005)^4 \left[\frac{1}{|r - 0.0015| + 1} - 0.996\right] \tag{20}$$

In (20), $\dot{Q}$ is the volumetric heating in W/m$^3$, $r$ is a radial distance from the origin, $z$ is a height from the origin, and $k$ is a variable gain constant. This function was developed with the heating at the top, but the function was evaluated with negative $z$ values in order to drive buoyancy induced flow dynamics from heating at the bottom of the drop.

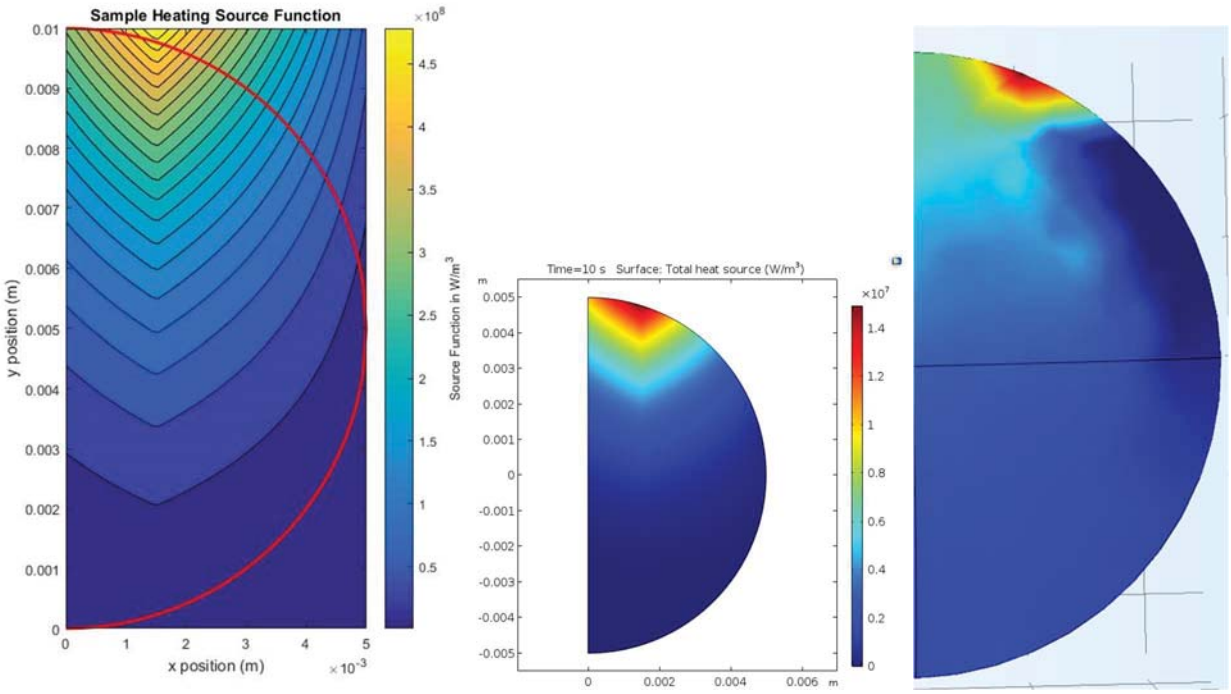


**Figure 15: Arbitrary continuous heating profile**

The leftmost image in Figure 15 shows a contour plot of the heating function generated in MATLAB, the center image is the heating function simulated by COMSOL, and the rightmost image is laser-heating contour generated from a coarse ray tracing simulation (included for comparison).

After developing this heating function, it was used in simulations to compare the MUMPS Solver against the PARDISO Solver, the Boussinesq approximation against Weakly Compressible resolution, and a segregated solution scheme against a fully coupled approach. These are all simulation parameters that can be selected in COMSOL.

These simulations highlighted that, unless there are reasons to deviate, simulations should stay with COMSOL's default settings. In the PARDISO-MUMPS comparison, the default, PARDISO, solved simulations slightly faster, but MUMPS used slightly less memory. This finding is consistent with COMSOL support documents. In the Boussinesq comparison, the Boussinesq approximation resolved faster, but the weakly compressible simulation had slightly different results, which are presumably more accurate since they include variable density as opposed to a force that approximates the effect of variable density. The segregated solver resolved faster than the fully coupled solver and they both converged to the exact same solution. The fully coupled solver is the default, so for some simulations, it may benefit to switch to a segregated solver.

**Continuous Heating Applied with Moving Mesh**

The continuous heating profile was also used for a Moving Mesh simulation that shows internal dynamics and changing domain volumes can be resolved simultaneously. Here, the

initial drop radius and the rate at which the drop radius decreased were specified. Four snapshots of the temperature profile for this heating and shrinking drop are shown in Figure 16.

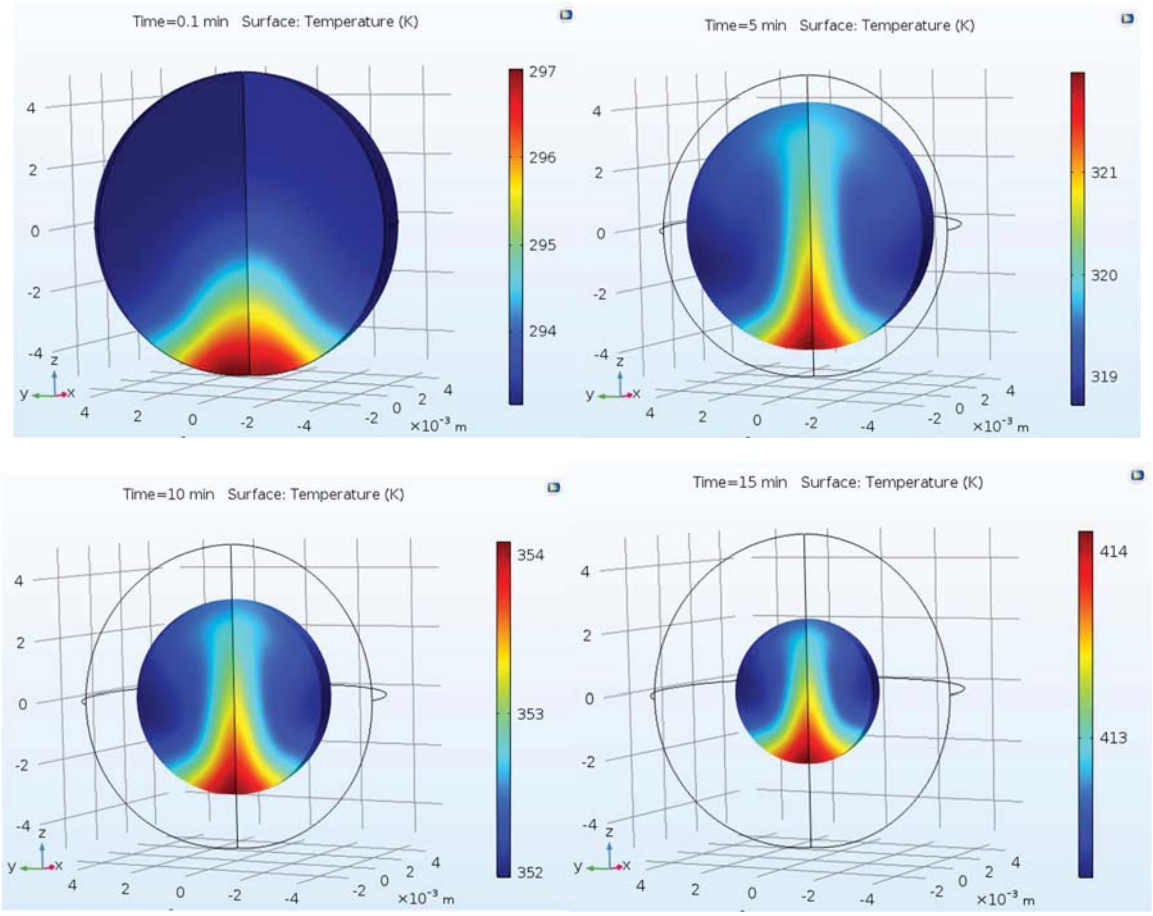


**Figure 16: Temperature profiles of moving mesh with continous arbitrary heating function**

In Figure 16, the temperatures on the color bar continually increases, so the drop is heating as it shrinks. The scales are not synchronized in order to show the temperature profile that develops. The drop appears isothermal throughout the simulation when the scales are synchronized. The heating is also not coupled with the changing drop radius. This moving mesh shows that a shrinking drop can be resolved in COMSOL, however, more considerations must be added in order to make this a realistic simulation.

# Three-Dimensional Non-Isothermal Flow

**Surface flux through a portion of the Drop**

The first simulation is a partial surface flux drop. This simulation highlighted the computational challenges involved in transitioning from two-dimensional to three-dimensional simulation. Here, one eight of the drop's surface area was defined with an arbitrary surface flux into it. This simulation used a high heat flux in order to generate significant internal motion. The 6.4 $MW/m^2$ corresponds to 640 $W/cm^2$, a realistic HEL irradiance. Exact parameters of this simulation are shown in Table 4. Select results from the simulation are shown in Figure 17.

**Table 4: Parameters for Eighth Surface Flux**

| Parameter | Value |
|---|---|
| Dimensions | 3D |
| Diameter | 1 cm |
| Initial Drop Temperature | 20℃ |
| Heat Flux through Drop Quarter | 6,400,000 $W/m^2$ |
| Mesh | Fine |
| DOF | 26,960 (plus 1075 internal DOFs) |
| Simulation time | 10 seconds |
| Solution time | 32 minutes 1 second |
| Time Steps | 260 |

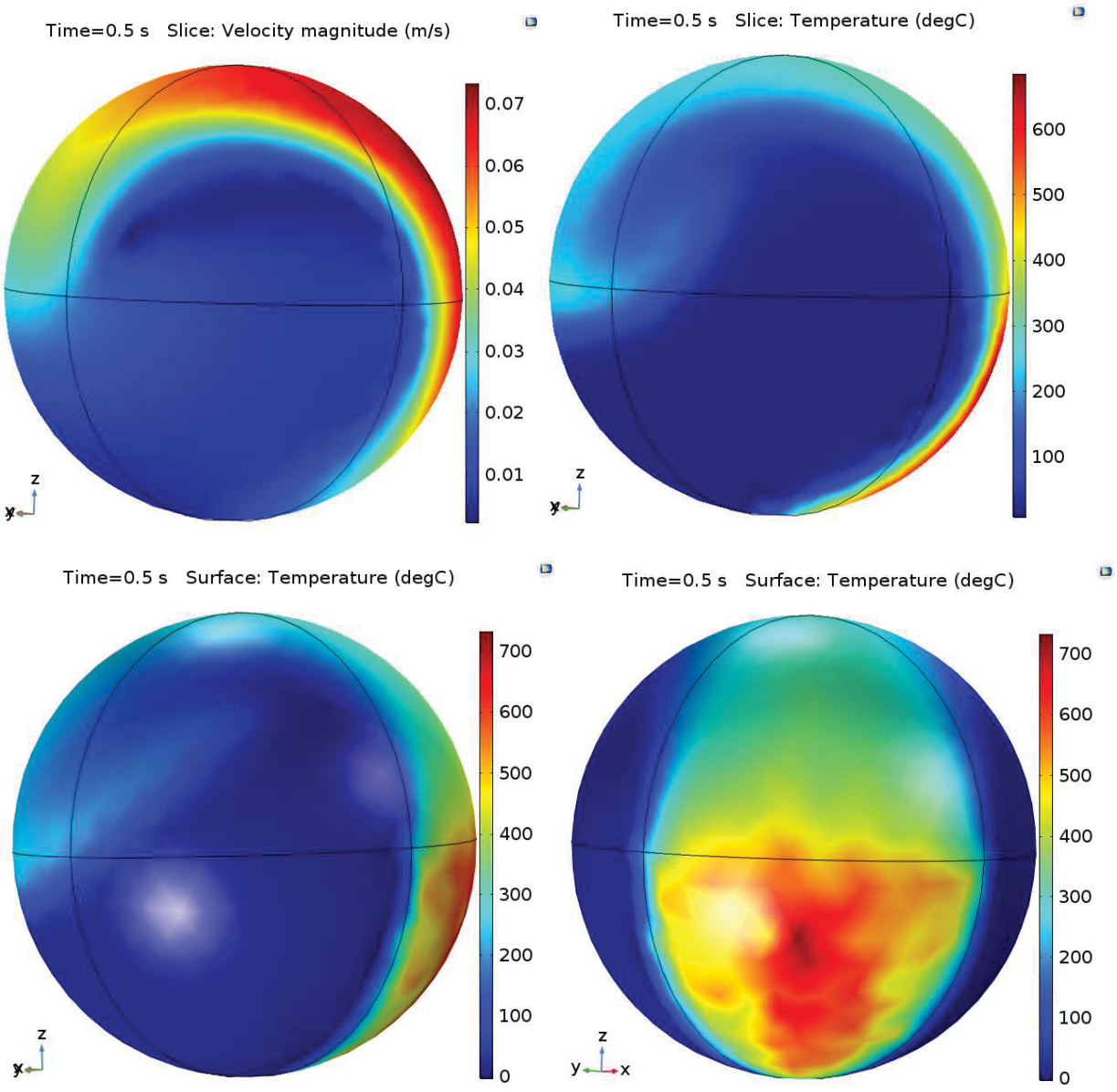


**Figure 17: Surface and slice temperatures for three-dimensional partial surface flux drop**

In Figure 17, the infeasible temperatures from this simulation and the resulting internal velocities are shown. After half a second of surface heating at 6.4 MW/m$^2$, the temperatures near the surface are already beyond the saturation temperature of water. Despite this fact, the drop simulation continues even though the physical meaning is lost. Once the drop has exceeded water's critical temperature at atmospheric pressure, it would spontaneously vaporize. With this heat flux, velocities of seven cm/s are reached almost instantaneously, which would rip the drop apart if it did not first vaporize. This simulation raises concerns regarding solution time. Most well posed two-dimensional studies resolved in under five minutes, but with a third dimension, the number of elements and degrees of freedom increase significantly faster as finite element meshes are refined.

**Heat Source as a function of x**

Since laser-heating profiles concentrate heating in the back of the drop, an analytic function was devised to help simulate heating profiles in three-dimensional drops. The goal of this simulation was to understand how an uneven aft-concentrated heating distribution within a three-dimensional drop would affect the internal dynamics. Exact parameters of this simulation are shown in Table 5. Select results from the simulation are shown in Figure 18.

**Table 5: Parameters for three-dimensional f(x) heated drop**

| Parameter | Value |
|---|---|
| Dimensions | 3D |
| Diameter | 1 cm |
| Initial Drop Temperature | 20℃ |
| Heat Function | $Q_{in}$= 200*(1,495*(x+.005))^4 [W/$m^3$] |
| Mesh | Fine |
| Discretization | P1+P1 |
| DOF | 85,247 (plus 1,078 internal DOFs) |
| Simulation time | 20 seconds |
| Solution time | 5 minutes 39 seconds |
| Time Steps | 45 |

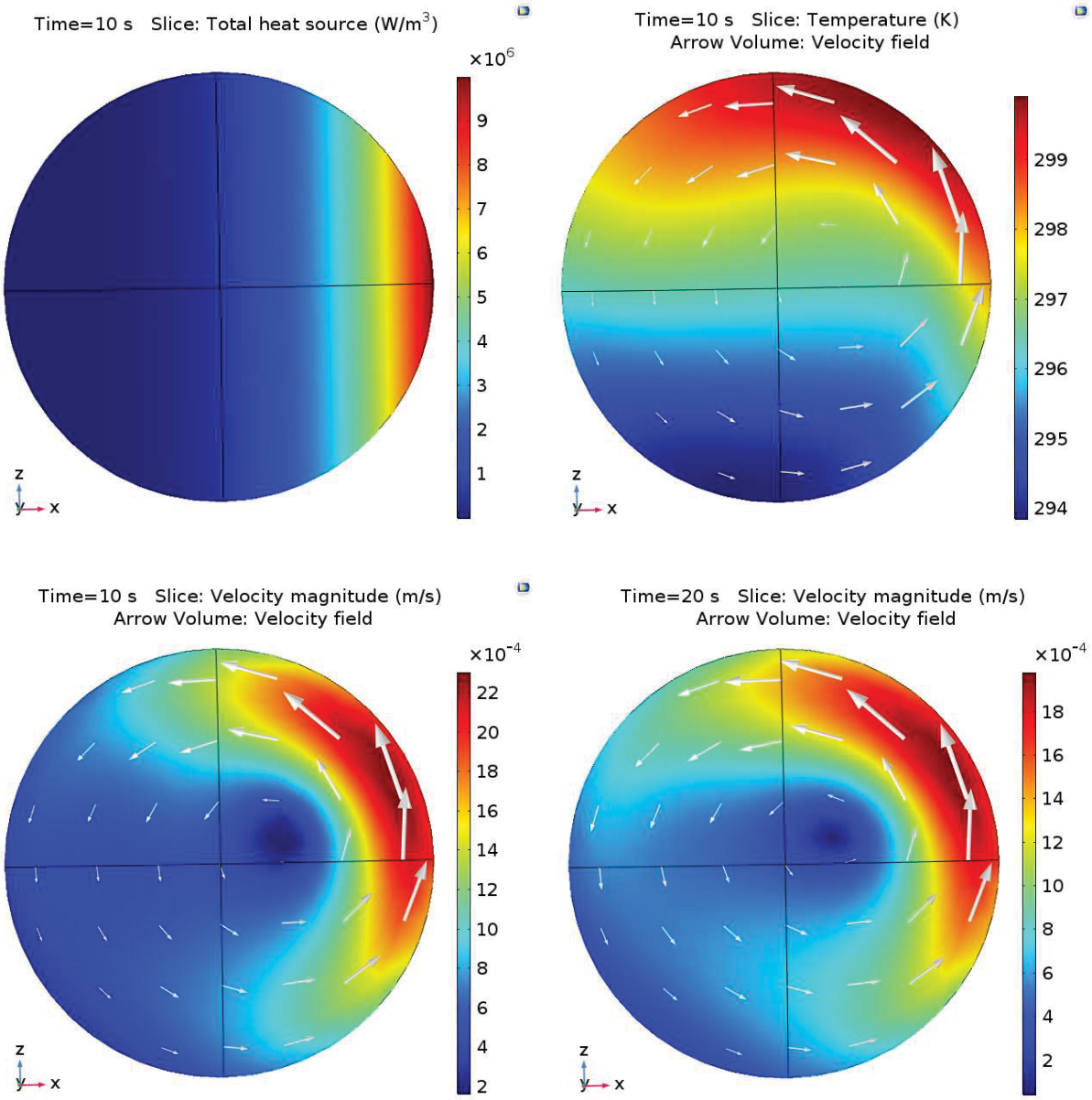


**Figure 18: Heat source, temperature, and velocity profiles for f(x) Heated Drop**

The results in Figure 18 show that this heating profile generates a maximum velocity of about 2 mm/s and this maximum velocity persists as the drop heats, maintaining a maximum temperature difference of approximately 6 °C. The maximum velocity magnitude and the average temperature within the drop are plotted in Figure 19. These quantities were obtained in COMSOL by defining domain probes, which record all the values within a given domain.

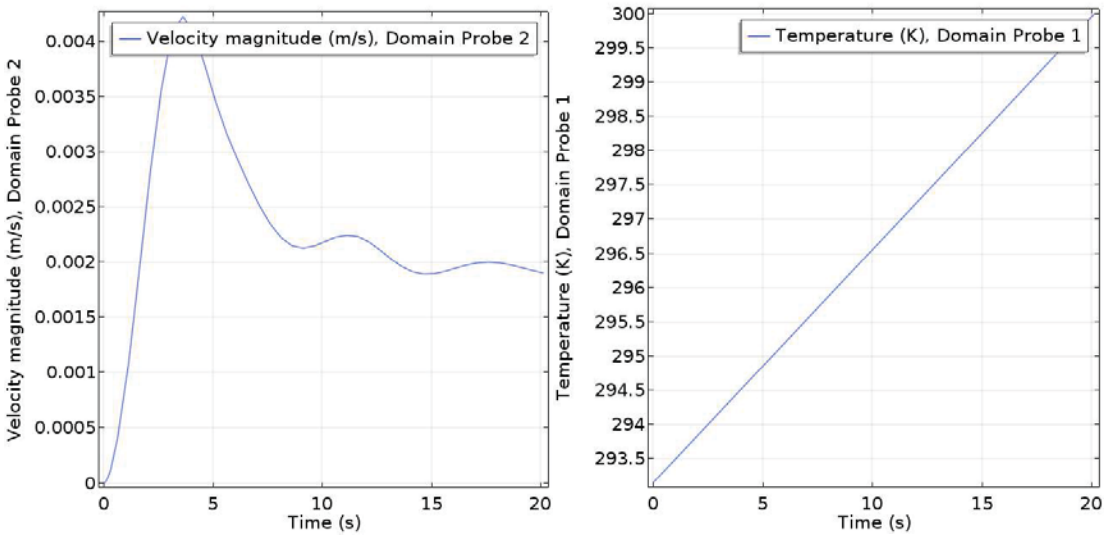


**Figure 19: Maximum velocity magnitde and average temperature in f(x) heated drop**

In Figure 19, the maximum velocity plot peaks at 3.6 seconds, then slows and stabilizes towards a lower value. This may occur due to a greater temperature gradient building while there is less motion and therefore the maximum velocity may represent a transition from diffusion to advection as the dominant mode of heat transfer.

Parameters and results for no stabilization simulations are shown in Table 6 and Figure 20

**Table 6: Parameters for f(x) heated drop P2+P1 discretization and no stabilization**

| Parameter | Value |
|---|---|
| Dimensions | 3D |
| Diameter | 1 cm |
| Initial Drop Temperature | 20℃ |
| Heat Function | $Q_{in}$= 200*(1,495*(x+.005))^4 [W/m$^3$] |
| Mesh | Fine |
| Discretization | P2+P1 |
| DOF | 162,572 (plus 1,078 internal DOFs) |
| Simulation time | 20 seconds |
| Solution time | 50 minutes 10 seconds |
| Time Steps | 45 |

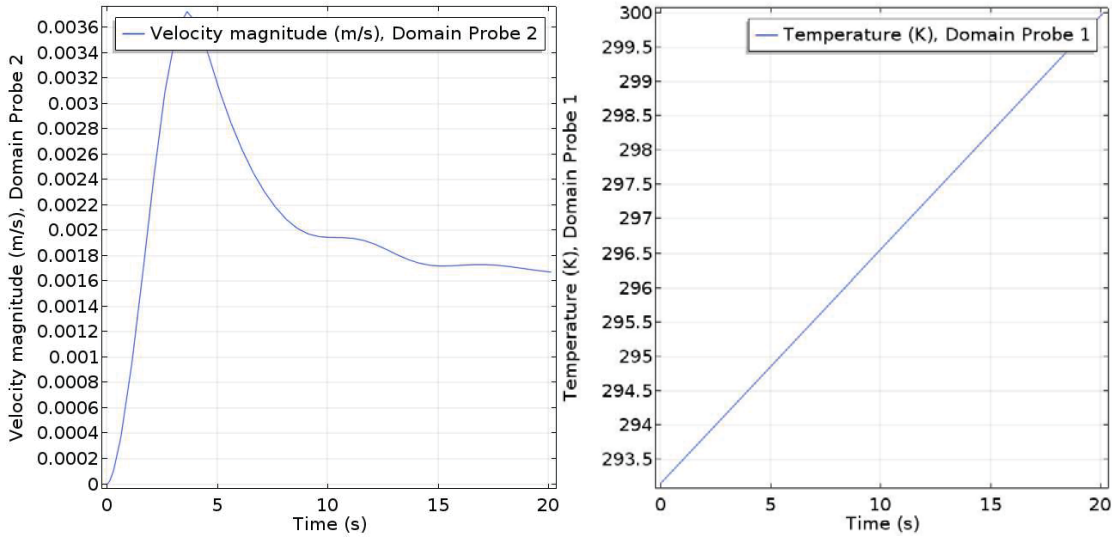


**Figure 20: Maximum velocity magnitde and average temperature in f(x) heated drop P2+P1 discretization and no stabilization**

The simulation conducted with stabilization has an average velocity magnitude that oscillates more than the simulation lacking stabilization. Based on further simulations, this is an artifact of the discretization order, not the stabilization. When the discretization P1+P1 is utilized, both pressure and velocity are resolved with first order polynomials whereas in P2+P1 discretization, pressure is resolved with first order polynomials while velocity is resolved with second order polynomials. Since the Navier-Stokes equation utilizes one derivative in pressure and two derivatives in velocity in the viscous term, as shown in (6), the Navier-Stokes Equation can only be resolved without stabilization when it is resolved at a P2+P1 discretization. [34]

## Laser Heat Field Applied to Drop

The laser heating profile shown in Figure 7 was applied to a three dimensional drop. This simulation helps illustrate the difference between heating as a function of x and heating that accurately represents the laser heating profile. Velocity snapshots for this simulation are shown in Figure 21.

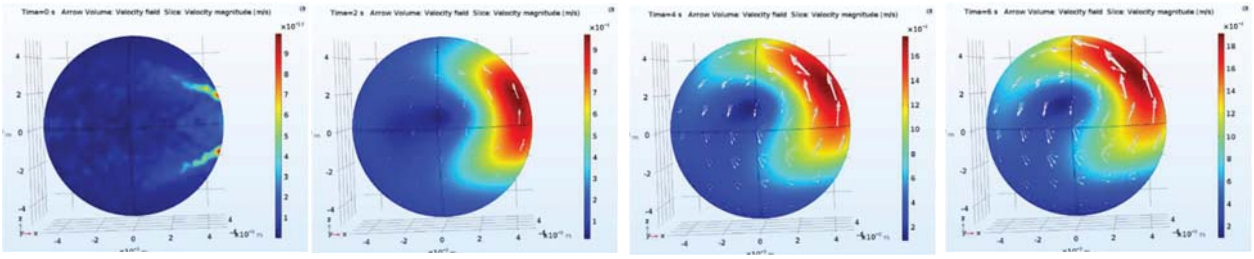

**Figure 21: Velocity profiles for a laser heated drop at t= 0, 2, 4, and 6 seconds**

The general shape of the velocity profile from the laser-heated drop qualitatively appears similar to the drop heated by a function of x. The same circular motion develops; however, in the laser heated simulation, the bottom of the higher velocity region extends more towards the center of

the drop. One crucial difference between these two simulations is the intensity of the heating. In the laser-heating scenario, the rays are focused by the drop, which forces the rays to converge in the area with the most heating, shown in Figure 7. In the drop heated by a function of x, the heating smoothly increases with x.

**Laser Heat Field with added Convection**

Since the dynamics of the drop with an applied laser heat field applied quickly reaches a steady state, a strong surface convection of 10,000 W/m$^2$-K was added to the drop to force a more dynamic response. 10,000 W/m$^2$-K was utilized because it is equivalent to the combined convection and vaporization heat removal from the experimental drop. To keep the maximum temperature in both simulations similar the heat function was increased by an order of magnitude in the drop with convection. Without convection, the temperature of the drop increases unconstrained; however, with convection, the drop will reach an average temperature at which the convective heat flux matches the volumetric heating from the laser. Figure 22 shows the temperature distribution comparison between the two heating cases. The heating function for the convected drop was increased by a factor of 10 to compensate for heat loss by convection.

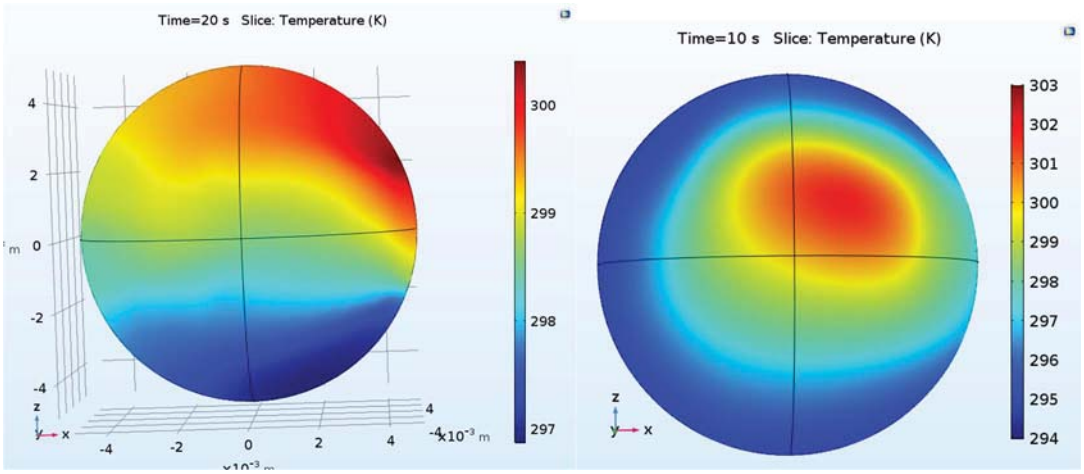


**Figure 22: Temperature profile for laser heated drop at 20 seconds (left) , and laser heated drop with convection at 10 seconds (right).**

The drop that is heated without convection reaches a steady state velocity due to the constant heat flux, but the temperature continues increasing. The drop with convection also reaches a steady state velocity as it approaches a steady state temperature. While convection simulates the evaporative cooling, this simulation still develops one central eddy which is not the behavior expected based on experiments [9]. A similar central eddy observed in the convection case can be seen in the case without convection shown in Figure 21.

**Varied Drop Shapes**

To simulate the effect of different drop shapes on the internal dynamics of the drop, a cube and ellipsoid domain were tested. In both domains, there were more eddies that resulted

from the different contours. For the cube simulation, the laser-heating function from the spherical drop was applied to a 1cm cube. The applied heat profile within the cube domain is shown in Figure 23.

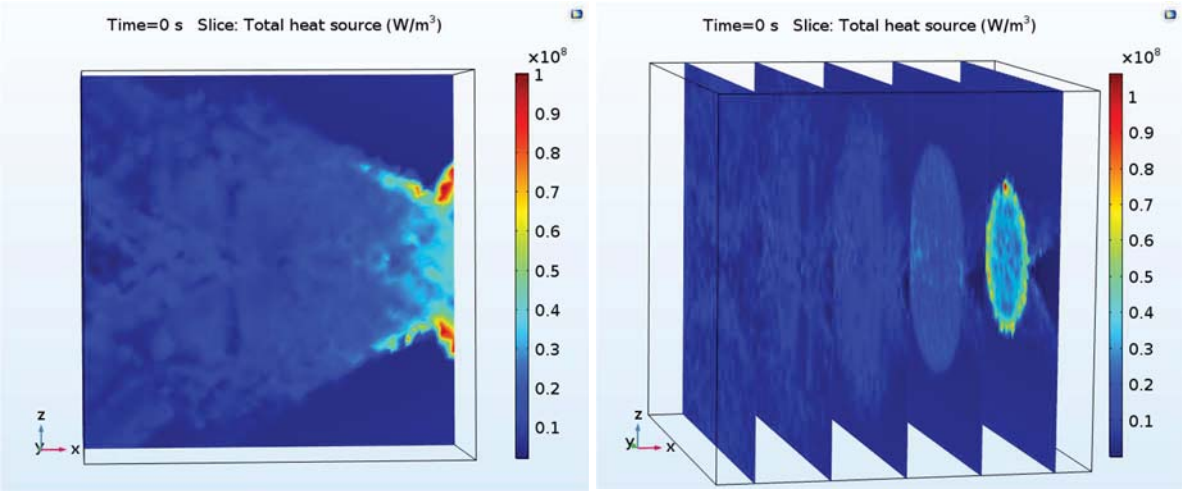


**Figure 23: Laser heat field from sphere ray tracing applied to cube shaped domain**

After applying the heating function, the simulation generated the temperature and velocity profiles. The sample profiles from a time of two seconds are included in Figure 24.

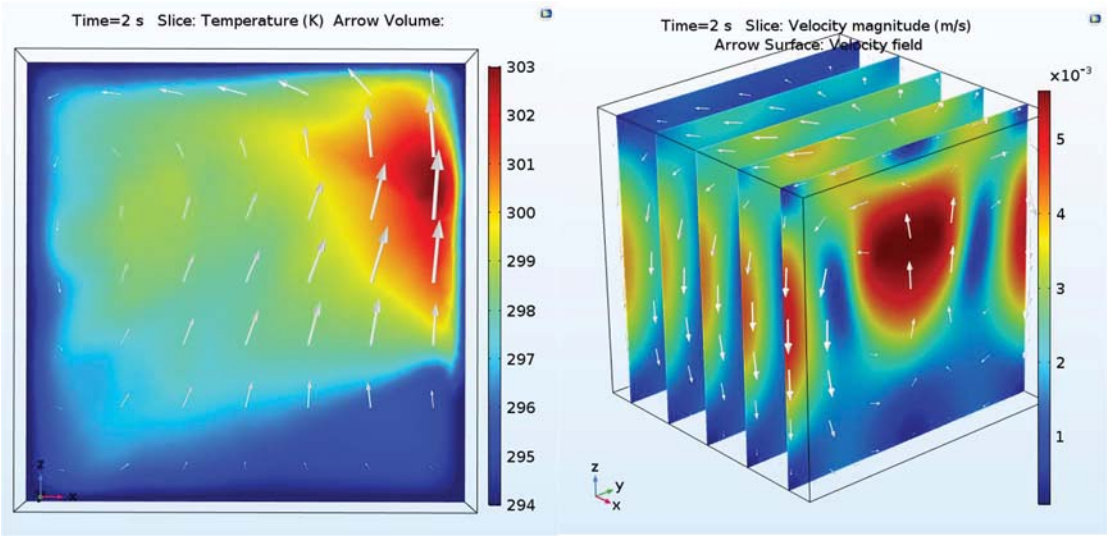


**Figure 24: Temperature (left) and velocity (right) profiles from a convected and heated water cube**

These profiles show the velocity vectors that circulate fluid upward in the back center of the cube domain, and bring it back down at the front and on the sides of the cube. This changes the internal dynamics from one eddy, in the spherical simulation, to a misshapen half vortex ring cut in half by the back surface of the cube.

The fluid dynamics in an ellipsoid domain with semi axes of 5 mm, 5 mm, and 2.5 mm was also simulated in order to explore a more realistic oblate-shaped drop. With the ellipsoid drop, ray-tracing simulations were conducted to generate a new heating profile. The heating profile generated is shown in Figure 25.

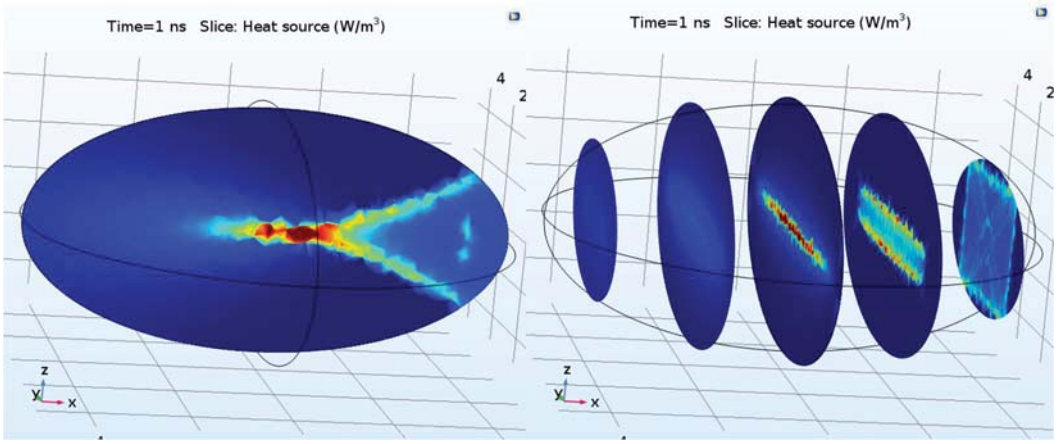


**Figure 25: Ellipsoid heating profiles generated from 40,000 rays incident on an extra fine mesh**

The heating field was then applied to a NITF simulation to resolve the internal fluid dynamics in the ellipsoid domain. Velocity profiles inside the drop with the laser propagating from the left (left image) and the laser propagating normal to the center of the drop (right image) are shown in Figure 26.

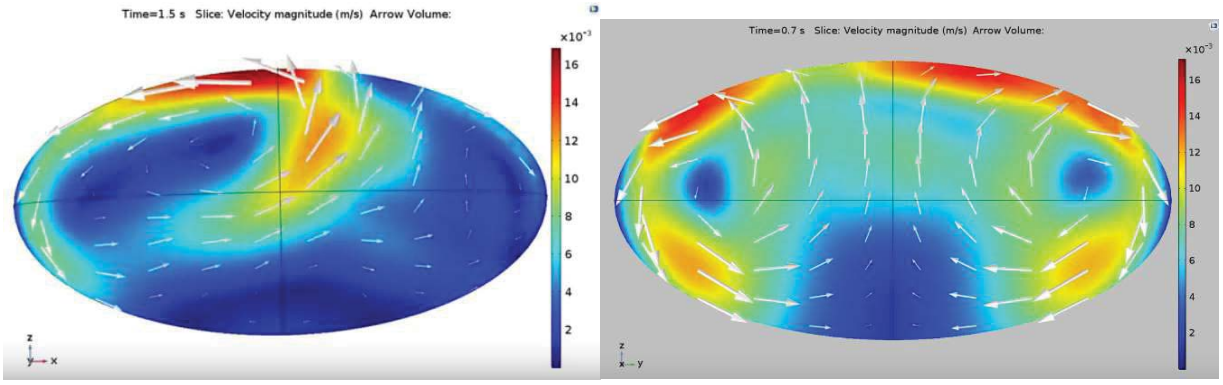


**Figure 26: Velocity profiles in ellipsoid domain at t=1.5 seconds with laser propagating from the left (left) and at t=0.7 seconds with laser propagating normal to the velocity profile (right)**

Based on the heating profile the maximum heating is concentrated just behind the midpoint in the ellipsoid. When the heated fluid rises to the right of the midpoint as shown on the left of Figure 26, the heated fluid is forced towards the left by the angle at the top of the ellipsoid. Some of the fluid is also forced to the right, which generates a vortex ring structure. This simulation generated more dynamics than the singular eddy of the spherical drop while maintaining a realistic drop shape. Similar to the spherical and cube shaped domains, it also approached a steady state velocity and temperature.

**Body Force Applied to Spherical Drop**

In order to generate internal drop dynamics that do not approach a steady state, a body forcing term was added to the simulation. This body forcing term is a coarse approximation for the impulses generated by the acoustic levitation. To generate the body force, a function was created in MATLAB to compute the velocity at discrete points within a two dimensional plane. The function applies a force to the fluid in the tangential direction and the magnitude of the force increases with the radius. The forcing function is shown in Figure 27.

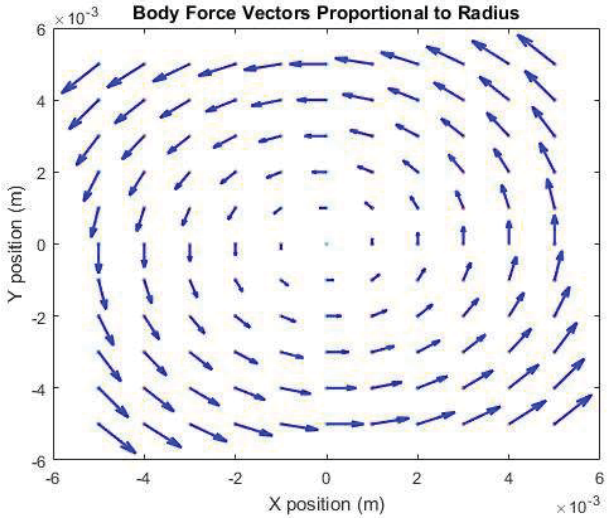


**Figure 27: MATLAB body force function = $\mathbf{F}_{tangential}$**

This body force was multiplied by a periodic function to force changing motion within the drop. The applied body function is shown in (21). A period of 2t was selected in order to generate smooth motion that would resolve in a reasonable amount of time. Greater forcing vatiations significantly increase computational time. The resulting velocity vector fields and temperature profiles are shown in Figure 28.

$$\mathbf{F}_{body} = \mathbf{F}_{tangential} \cdot \sin(2t) \tag{21}$$

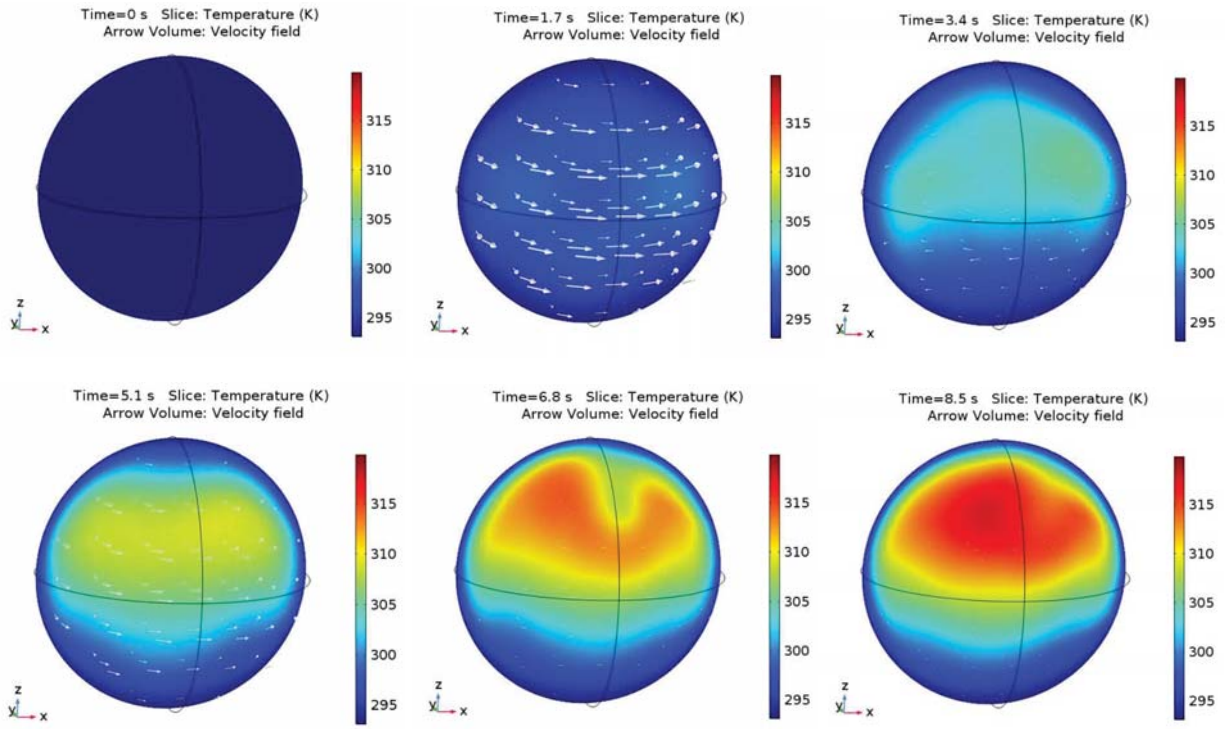


**Figure 28: Temperature profiles and velocity fields for laser-heated drop with convection and body forcing fucntion**

# Scaling Heating Profile

**Imaginary index of refraction**

In order to control drop heating as the imaginary index of refraction, or absorptivity, varied and drop size decreased, a parametric sweep of various water thicknesses and imaginary indices of refraction were tested to determine transmittance through water. The transmittance results are shown in Figure 29.

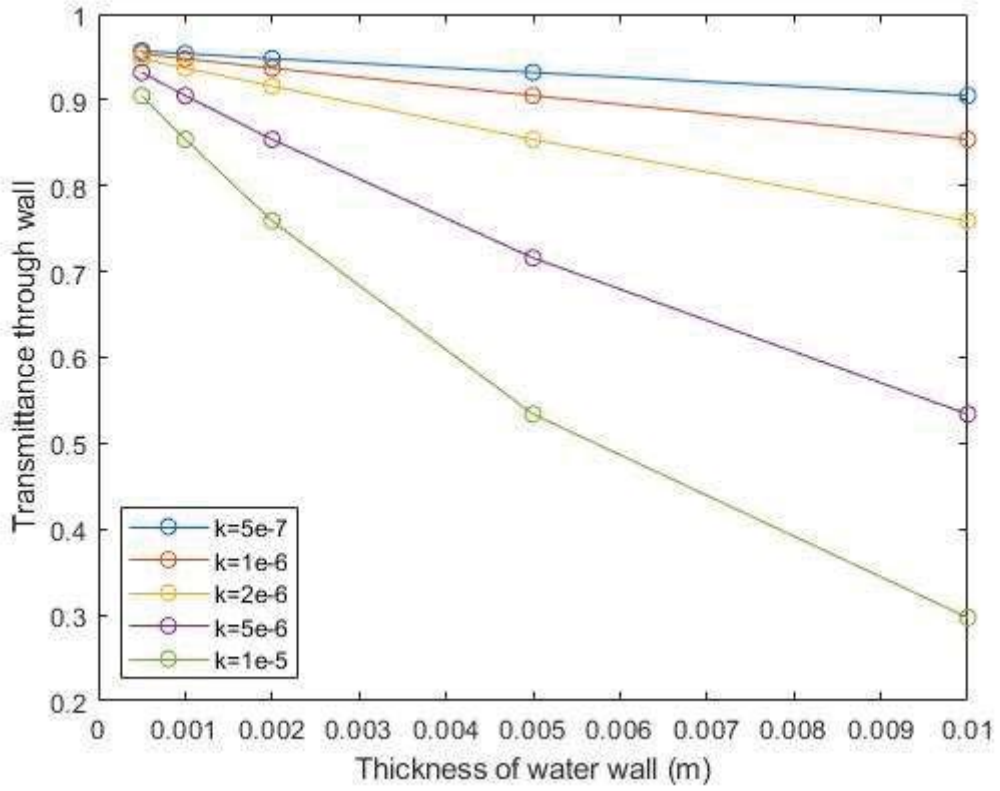


**Figure 29: Transmittance for varied imaginary indicies of refraction**

After conducting an exponential regression of the transmittance, the results were tabulated in Table 7.

**Table 7: Exponential regression of transmittance through water wall**

| Imaginary index of refraction | Exponential regression of transmittance |
|---|---|
| 5E-7 | $T=.96e^{-5.86x}$ |
| 1E-6 | $T=.96e^{-11.6x}$ |
| 2E-6 | $T=.96e^{-23.4x}$ |
| 5E-6 | $T=.96e^{-58.6x}$ |
| 1E-5 | $T=.96e^{-117.3x}$ |

Table 7 shows that as the thickness approaches zero, the transmittance approaches 96%. Fresnel's law explains this concisely as seen in (20).

$$R_s = \left[\frac{n_1 cos\theta_i - n_2 cos\theta_t}{n_1 cos\theta_i + n_2 cos\theta_t}\right]^2 \quad (20)$$

Evaluating the reflectivity of an air water interface with incident and transmitted angles of 90 degrees and refractive indices of 1 and 1.333 respectively, the reflectivity evaluates to 2.04%. With two surfaces to reflect off of, the total reflected is approximately 4% and the transmitted irradiance is about 96% as the wall thickness approaches zero. The relationship between imaginary index of refraction and extinction coefficient is shown in Figure 30.

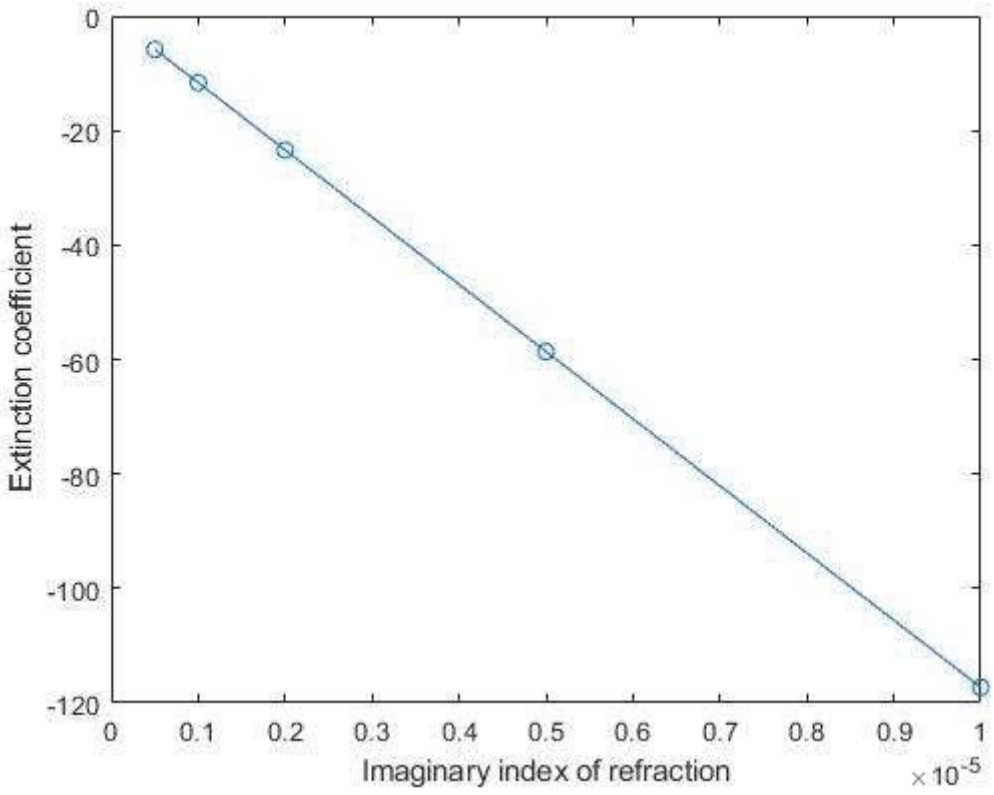


**Figure 30: Extinction coefficient at varying imaginary indicies of refraction**

Figure 30 shows that the imaginary index of refraction and the extinction coefficient are directly proportional. To more directly evaluate the effect of varying the imaginary index of refraction on the heating field of a drop, the imaginary index of refraction for 1064nm of k=1.27e-6 was varied in a parametric sweep with six different drop sizes to determine how average heating varies as drop size changes and as the imaginary index of refraction is varied. The average heating results are shown in Figure 31.

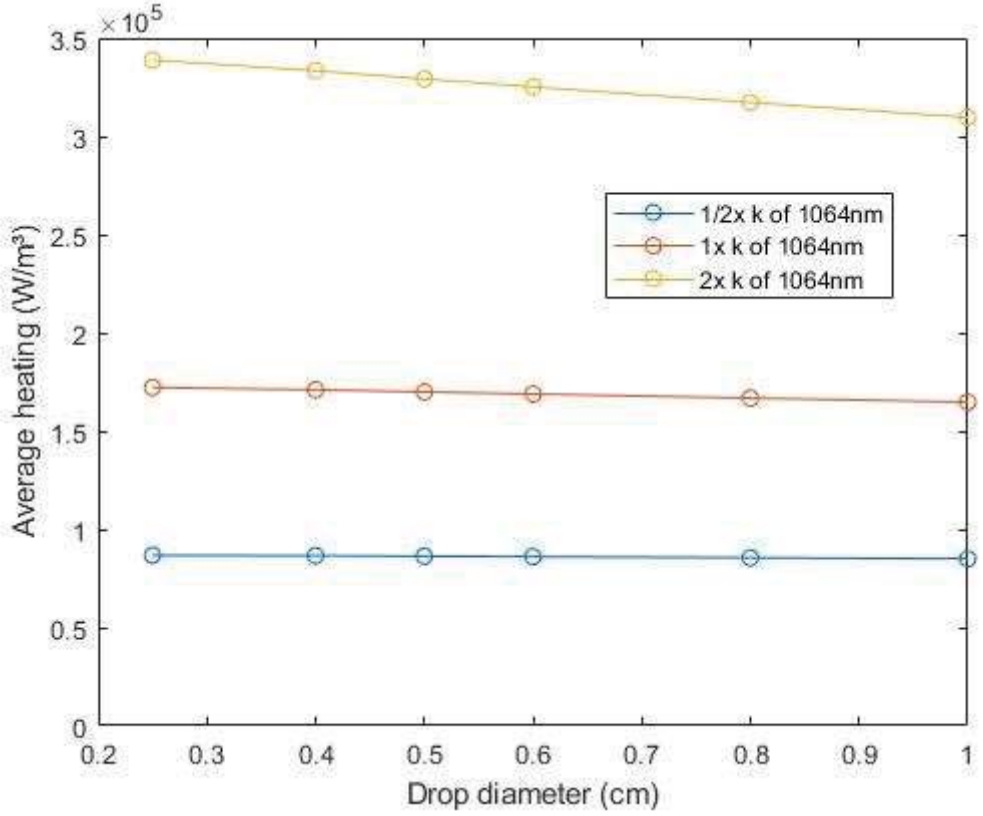


**Figure 31: Variation in heat profile with varied size and imaginary index of refraction**

In Figure 31, doubling the imaginary index nearly doubles the average heating. As drop size decreases, the average heating slightly increases. This is due to the fact that as rays propagate through a drop, they lose energy so the back of the drop does not receive as much heating from the rays as the front. As the drop shrinks; however, this effect is diminished. This effect is more prominent for larger indices of refraction. Since size plays a small role in changing the average heating of the drop, its effects were not included as the heating field scaled with the drop.

**Heating field setup**

The heating field generated using geometrical optics was scaled with the shrinking drop by using the radius at any given time step to determine the heating field. In order to scale the heat field, the heat source was scaled in accordance with (21).

$$Q_{src} = Q_{ht}\left(\frac{x \cdot R_0}{r}, \frac{y \cdot R_0}{r}, \frac{z \cdot R_0}{r}\right) \cdot \frac{r^3}{R_0^3} \tag{21}$$

In (21), $Q_{src}$ is the heating function applied to the drop, $Q_{ht}$ is the imported heat field from another drop simulation, r is the instantaneous drop radius, and $R_0$ is the original drop radius. The *x*, *y*, and *z*, arguments in (21) pull heating values closer to the origin as the drop shrinks. The cubic argument maintains a constant magnitude. In Figure 32, the drop heating profile for the validation test case is shown at t=5 seconds, and t=25 seconds.

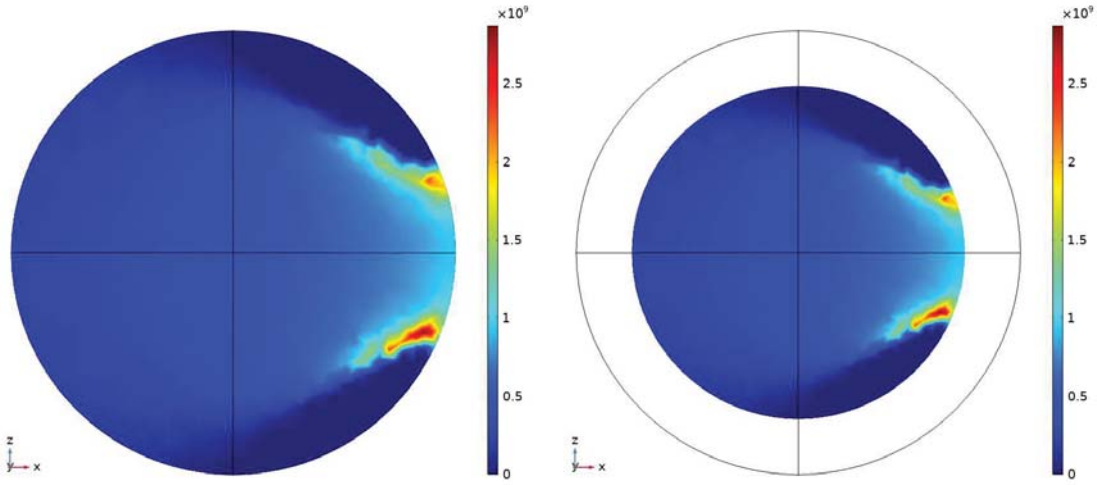


**Figure 32: Heat field in shrinking drop at t=5 seconds (left) and t=25 seconds (right)**

**Moving mesh**

In order to model drop shrinking, a moving mesh was defined. To activate the moving mesh, the entire drop was selected as the deforming domain, and a prescribed normal mesh velocity derived from experimental recordings was used. The rate of drop shrinking as determined by [9] is given in (22).

$$\frac{dr}{dt} = -0.0145 \cdot r \cdot step5(t) \tag{22}$$

In (22), *step5(t)* is a step function that begins at a time of five seconds. This five second time delay was implemented to account for an initial heat up period before drop vaporization began. The experimental volume from [9], and a volume probe from the validation model are both shown in Figure 33.

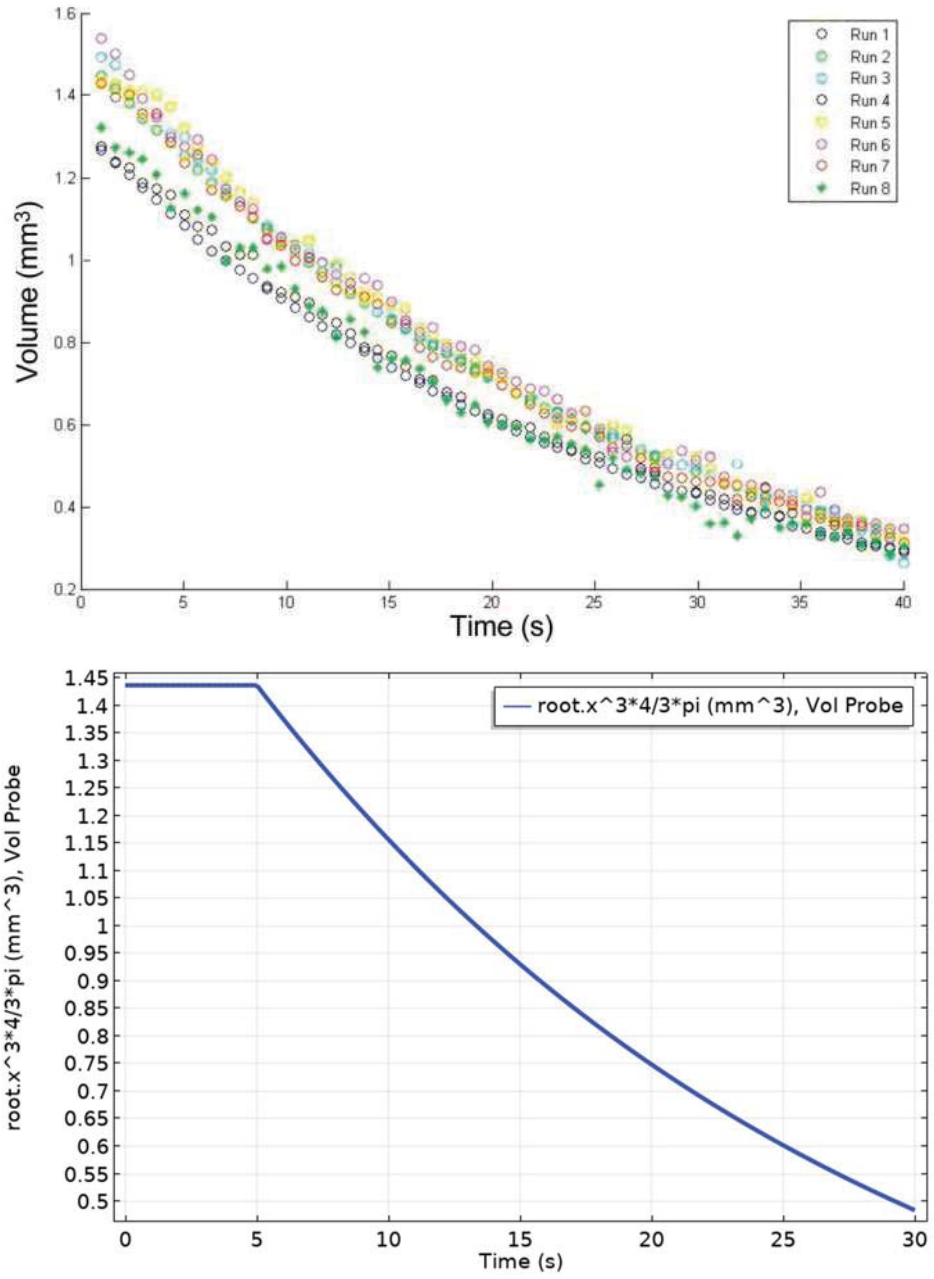


**Figure 33: Experimental (top) and simulated (bottom) drop volume of laser-irradiated drop**

While the moving mesh enabled the resolution of a shrinking drop, it complicated the results by creating an instability at the pressure point constraint. The pressure point constraint is required in COMSOL CFD simulations in order to have a fully defined model. The pressure at the top of the drop was set to atmospheric pressure, and the pressure throughout the rest of the drop varied with respect to this baseline pressure. In Figure 34, the "finer" mesh used for the validation model is shown.

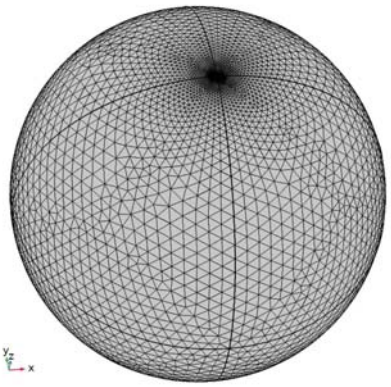

**Figure 34: Validation model mesh with refined pressure point constraint**

The pressure point constrain was refined with a maximum element size of 2.8E-6 in order to suppress the chaotic motion near the pressure point constraint.

**Realistic convection and mixing**

With drop shrinking refined and the scaled heating profile in place, a parametric sweep of convection coefficients was run to determine the ideal convection coefficient. A convection coefficient of 1600 W/m$^2$-K was initially chosen, while the forcing was determined. In order to apply forcing to the drop, a rotating gravity field was applied. This rotating body force introduced pseudo-stochastic forcing that would be generated by acoustic levitation, or turbulent oscillations from freefall. Uniform acceleration in the x direction varied with *cos(t)* while acceleration in the y direction varied with *sin(t)*. A parametric sweep of various magnitudes and periods of oscillation was conducted to determine the ideal combination of frequency and magnitude. A magnitude of three times gravity was selected, but the resulting drop surface temperatures appeared artificial, so a pseudo-stochastic approach to forcing was implemented. Since a summation of sines and cosines yields a seemingly chaotic, less predictable forcing magnitude, (23) was used as the internal forcing to develop motion that emulated the forcing from the acoustic levitation device. Furthermore, the direction of mixing appears to change within the experimental drop, so the final validation model incorporates pseudo-stochastic forcing that turns off, and resumes rotating in the opposite direction. The equations used for forcing are shown in (24).

$$\begin{aligned} A_x &= \mathrm{step0}(t)\mathrm{k}\cdot\mathrm{g}\cdot(\cos(\emptyset t)+\cos(3\emptyset t)+\cos(5\emptyset t)-\mathrm{step10}(t)(per)\ldots \\ &\quad +\mathrm{step15(t)}(per) \\ A_y &= \mathrm{step0}(t)\mathrm{k}\cdot\mathrm{g}\cdot(\cos(\emptyset t)+\cos(2\emptyset t)+\cos(7\emptyset t)-\mathrm{step10}(t)(per)\ldots \\ &\quad +\mathrm{step15(t)}(per) \\ A_z &= \mathrm{step1}(t)(-g+g\cdot\sin(\emptyset t)) \end{aligned} \tag{24}$$

In (24), the step functions represent the initial on at t=0, the forcing stop at t=10 seconds, and the forcing resume at t=15 seconds. The "*per"* that appears nest to the step functions represent the cosines with various frequencies because they are all turned off and on together. The k magnitude was set to three to more magnify the rotating acceleration field, and ∅ was set to *pi/2*.

# Validation model

## Validation model setup

The parameters used for the validation model are shown in Table 8.

**Table 8: Parameter used in validation model**

| Parameter | Value |
|---|---|
| Dimensions | 3D |
| Diameter | 1.4 cm |
| Initial Drop Temperature | 20℃ |
| Heat Function | Scaled from ray trace of 1000 W/cm$^2$ 1064nm |
| Mesh | Fine with refined pressure point constraint: max element size of 2.8e-6 |
| Discretization | P1+P1 |
| DOF | 357,728 (plus 512,021 internal DOFs) |
| Simulation time | 30 seconds |
| Solution time | 4 hours, 4 minutes, 5 seconds |
| Time Steps | 466 |

All material properties for water came from the COMSOL material library. The 1.4 mm diameter drop had an initial temperature of 20 °C with no internal motion. A slip boundary condition was set on the surface as well as a 1600 W/m$^2$-K convection coefficient. To couple the internal motion with the laser heating, the Boussinesq approximation was applied. P1+P1 discretization was utilized because while it requires stabilization to resolve the simulation, P1+P1 discretization has many fewer degrees of freedom than P2+P1 and it therefore reduces the computational time significantly. The moving mesh defined drop shrinking in accordance with the model matched to experimental results in [9]. Drop shrinking starts at 5 seconds, the forcing stops at 10 seconds, and it resumes in the opposite direction at 15 seconds. The volume and surface temperatures results of the validation model can be seen in Figure 35. For all the resolved simulations, surface temperature was evaluated by using the surface temperature of the front right quarter of the drop surface. The front of the drop is the side where the laser is incident. This area was selected for simplicity because COMSOL sets default boundary breaks in the x, y, and z planes that separated the drop surface. The volume max, min, and average temperatures were calculated by evaluating the temperatures throughout the entire drop domain.

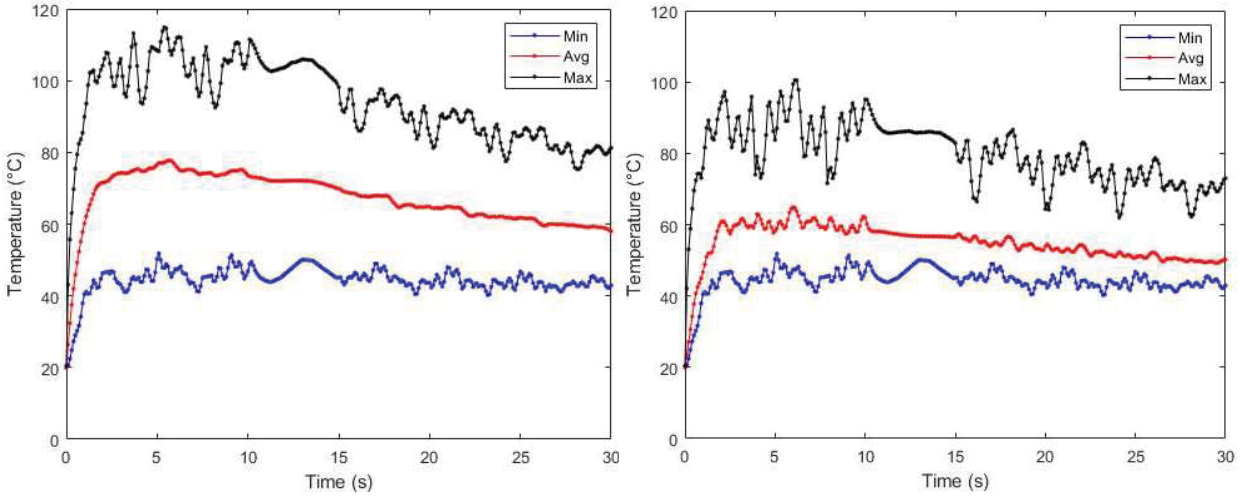


**Figure 35: Volume (left) and surface (right) temperatures for validation model**

The volume max and average temperatures are much higher for the volume than they are for the surface, however, since the volume includes the surface, the minimum temperatures are nearly identical. This is because heat loss occurs at the surface of the drop due to the applied convection coefficient. The oscillations in all the temperatures in the last fifteen seconds of the simulation appear to be periodic in nature which is a direct result of the sudo-stochastic forcing shown in (24). At ten seconds when the forcing stops, the temperature fluctuations drastically decrease, but they resume promptly at fifteen seconds when the forcing resumes. In Figure 36, the volume velocities of the validation test case are plotted.

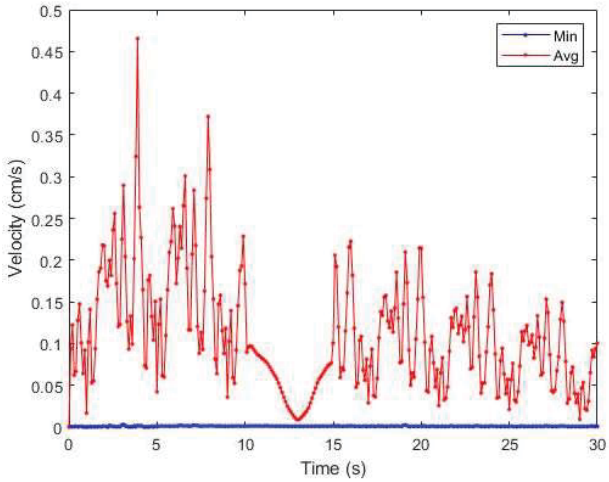


**Figure 36: Volume velocities for the validation test case**

The maximum velocity plotted (left) in Figure 36 shows that the maximum velocity spikes when the drop begins shrinking. The location of the maximum velocity was consistently in the vicinity of the pressure point constraint. The mesh around the pressure point constraint was refined in

order to reduce the effect of the point boundary condition; however, the refined mesh reduced the distance the instabilities reached out; however, the magnitude of the maximum velocities did not vary noticeable with a finer mesh. Figure 36 adds confidence in the validation test case, because in a 1.4 mm drop, experimentally motion was visually close to the simulated average values. The minimum velocity will always be approximately zero because within any vorticity field, there will be a location where the velocity approaches zero.

# Test Matrix Results

**Table 9: Test Matrix**

| Varied Parameter | Fluid | Diameter | Intensity | Wavelength |
|---|---|---|---|---|
| **1. Validation** | Water | 1.4 mm | 1000 W/cm$^2$ | 1064 nm |
| **2. Size** | Water | 100 µm<br>1 mm<br>5 mm | 500 W/cm$^2$ | 1064 nm |
| **3. Intensity** | Water | 1 mm | 500 W/cm$^2$<br>5 kW/cm$^2$<br>50 kW/cm$^2$ | 1064 nm |
| **4. Wavelength** | Water | 1 mm | 500 W/cm$^2$ | 532 nm<br>1064 nm<br>10 µm |
| **5. Viscosity** | 1/2x µ water<br>1x µ water<br>2x µ water<br>16x µ water | 1 mm | 500 W/cm$^2$ | 1064 nm |

**Varied drop sizes**

To evaluate the effect of drop size on temperatures, and internal motion, three drop sizes were tested. Only the initial radius, defined in the global parameters, was varied for each run of the simulation. The data from the simulations was then exported to a table using the COMSOL developer commands included in Appendix F. The max and average drop temperatures for the three tested drop diameters are shown in Figure 37.

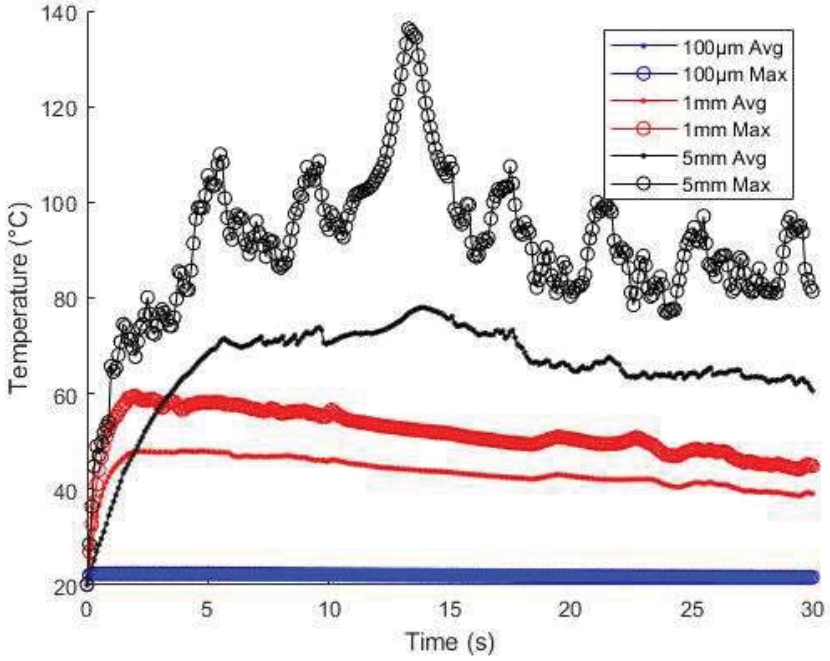


**Figure 37: Max and average temperatures for varied drop sizes**

Figure 37 shows that as drop diameter increases, the average and maximum temperature within the drop also increase. This is a direct result of the surface area to volume ratio. As the diameter of a sphere increases, the surface area to volume ratio decreases which leaves less space for convection to occur. Of note in Figure 37, the temperature of the 5 mm drop increases dramatically when the forcing is stopped. This highlights the importance of internal motion within the drop to drive the cooling process. If the simulation did not include any forcing, than the temperatures for the entire simulation would all be higher: especially for larger drop diameters. The average velocities resulting from the internal heating and forcing are shown in Figure 38.

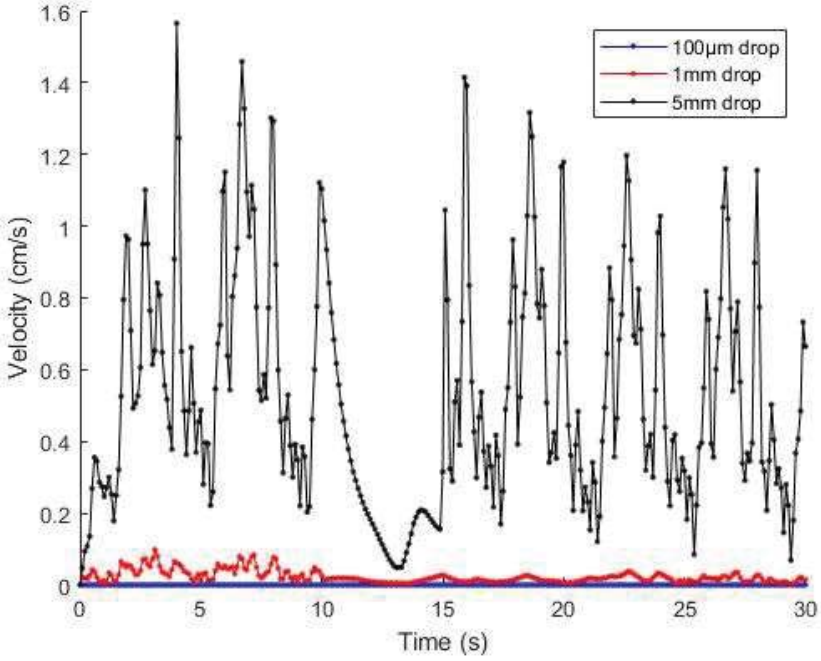


**Figure 38: Average velocites for various drop sizes**

The average velocity within the larger drops is much higher than the average velocity for the smaller drops. This is due to the fact that viscous dissipation is greater for smaller scales of motion. In the smaller drops, large eddies and whorls cannot exist, so the small eddies are quickly dissipated resulting in low maximum velocites. In larger drops however, there is more room for larger eddies to develop which enabel greated internal velocities. To also compare the effect of varying drop size with temperature, Figure 39 shows drop temperature as a function of temperature.

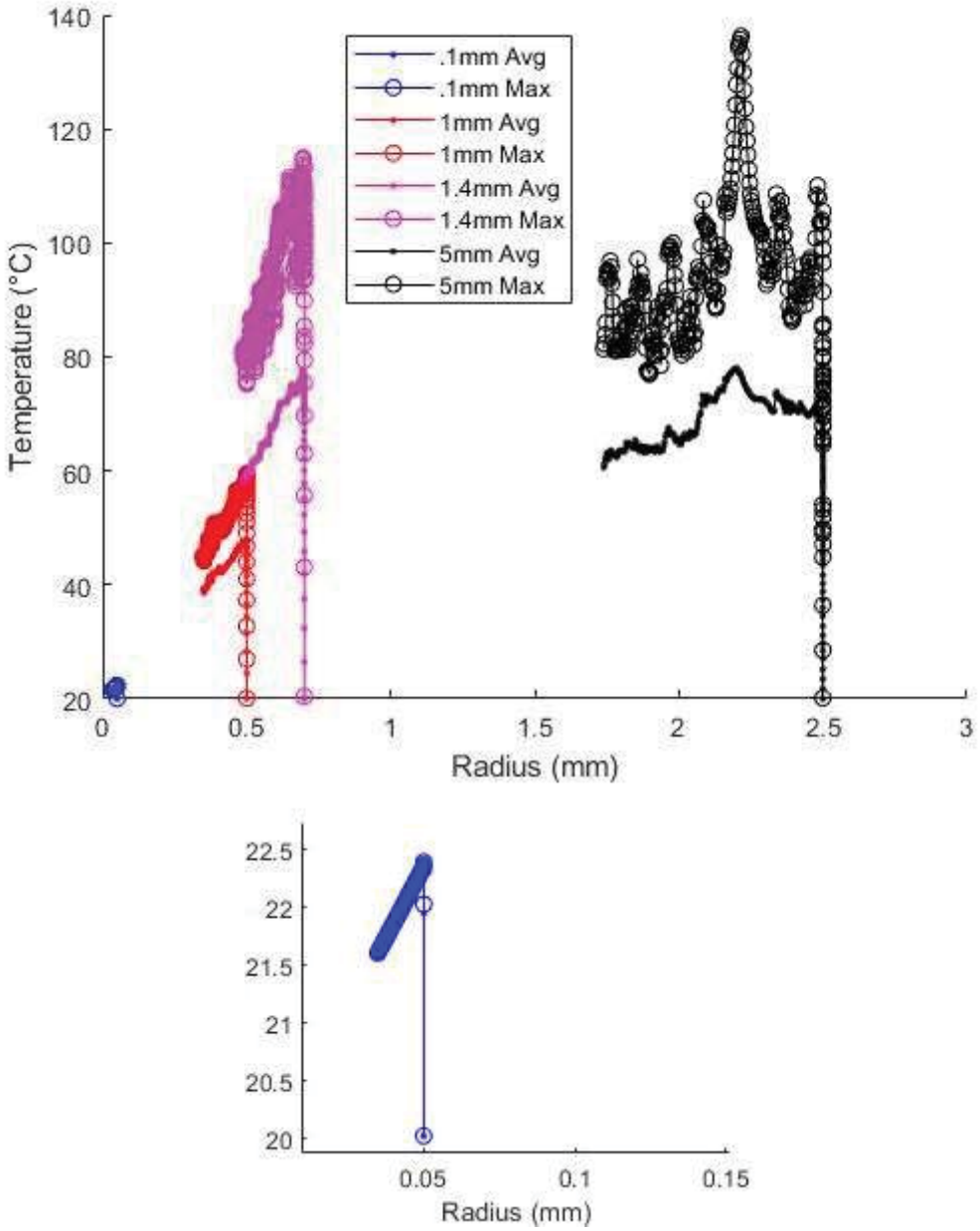


**Figure 39: Drop temperature at varied drop radii**

In Figure 39, as the radius decreases, the drop temperature also decreases. The 1.4 mm drop is the validation test case which was irradiated by 1000 W/cm$^2$ as opposed to the 500W/cm$^2$ incident on the other three drops. The effect of size on average velocity is shown in Figure 40. The slope of the temperature with respect to drop radius suggests that mixing and the surface area to volume ratio both play a large role in governing the temperature within the drop. For the 5 mm drop, when the forcing stops, the maximum and average temperatures both spike; however, this trend is not easily observed in the 1 mm or 1.4 mm drop. For the 100 µm drop,

there is no observable effect from the forcing whatsoever. This indicates that the internal motion within larger drops must be resolved in order to determine internal temperatures to any degree of accuracy.

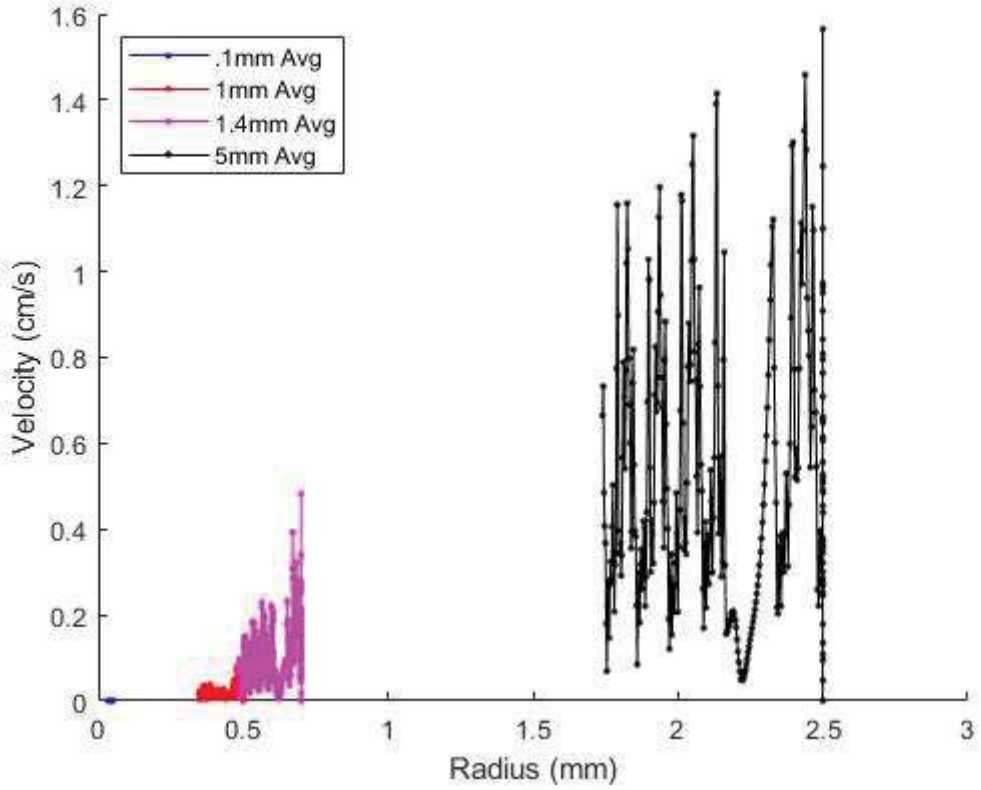


**Figure 40: Effect of size on average internal drop velocity**

In Figure 40, the average velocity magnitude increases with drop size. In this plot, the 1.4 mm diameter drop received double the incident irradiance. The general trend shows that as the radius approaches 0.5 mm, the motion quickly dampens out. At radii much smaller than 0.5 mm, the internal behavior becomes almost laminar.

### Varied irradiance

In order to extrapolate the effects of laser vaporization to higher energy lasers based on the validation model, higher irradiances were simulated within 1 mm shrinking drops. The average temperatures of these drops are shown in Figure 41.

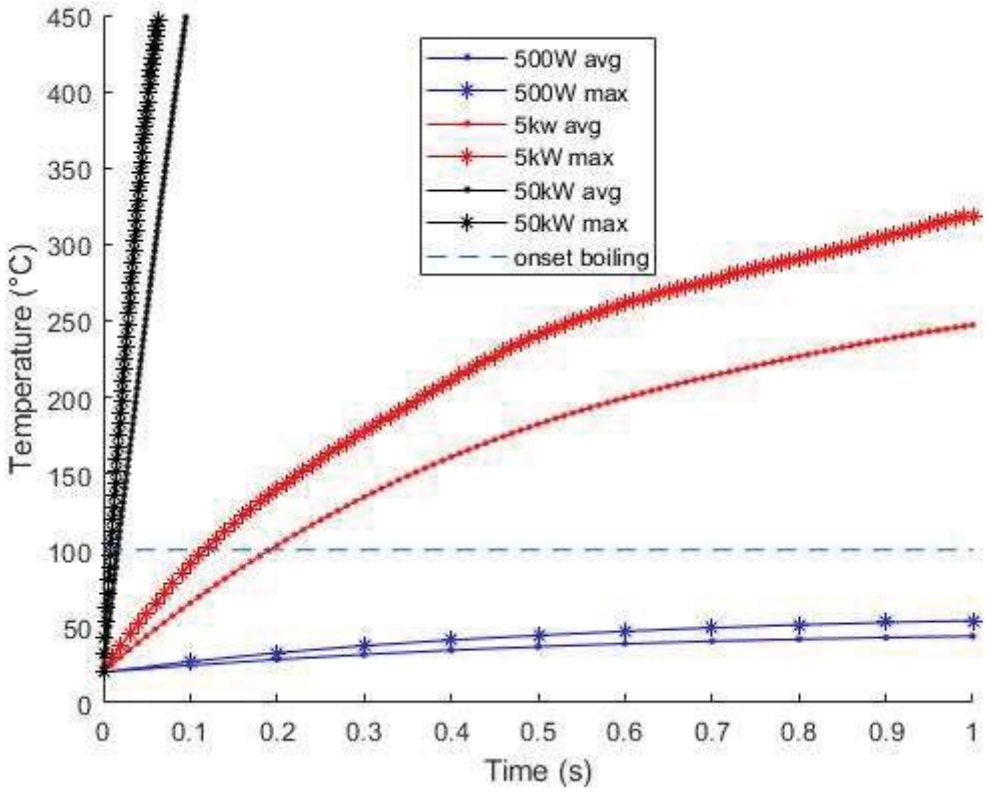


**Figure 41: Temperature of drops exposed to varied irradiances**

Figure 41 shows that as irradiance increases, the rate of heating also increases. At 500 W/cm$^2$ the drop is still in the slow heating regime, but as the irradiance increases to 5 kW/cm$^2$ and 50 kW/cm$^2$, the drop will certainly vaporize and explode within fractions of a second for the 5 kW/cm$^2$ case, and within only a few milliseconds for the 50 kW/cm$^2$ case. The 500 W/cm$^2$ drop never reaches 100°C, but the 5kW and 50 kW case take 0.12 seconds, and 0.009 seconds respectively. The average drop temp for the 5kW and 50kW case reach 100°C in 0.20 seconds and 0.017 seconds respectively. The average volume velocities for these test cases are shown in Figure 42.

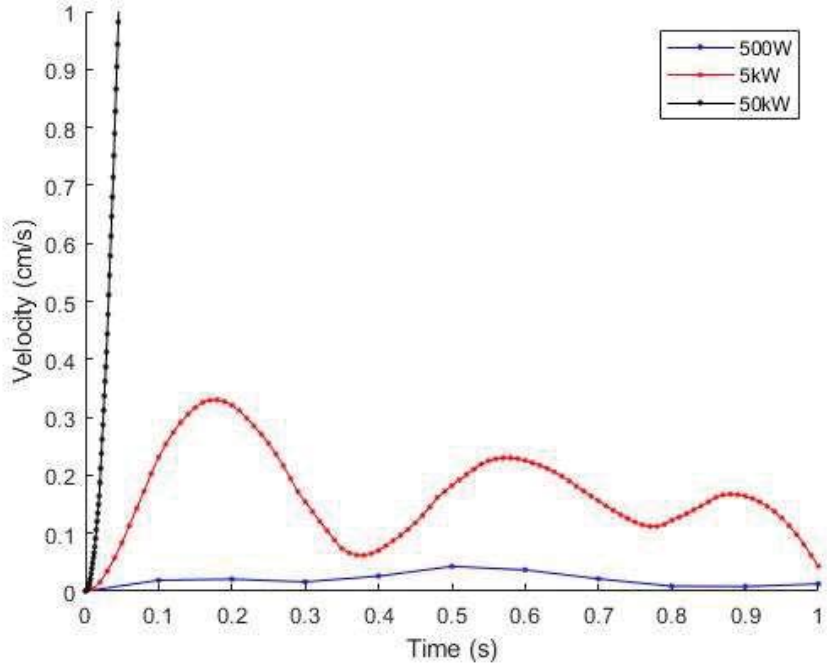


**Figure 42: Average velocites for 1 mm drop at varied irradiances**

Figure 42 shows that immediately there is significant motion in the drop exposed to the highest irradiance, while the drop exposed to the lowest irradiance did not have significant motion. The drop exposed to 5 kW/cm$^2$ showed oscillatory average velocities due to a combination of the rotating gravitational field, and great enough temperature gradients to drive buoyancy induced motion.

**Varied wavelengths**

To test the effect of varied wavelengths, 532 nm, 1064 nm, and 10 µm radiation were all tested on a 1 mm drop. Because the absorptivity water varies with wavelength, new heating fields needed to be generated to implement them into the non-isothermal flow simulations. For the 532 nm case, the imaginary index of refraction is 1.74E-9 which is approximately 730 times less than the absorptivity for 1064 nm at 1.27E-6. Because there is little relative attenuation for either of these wavelengths, the same heat field was applied for both except the magnitude of the heating for 532 nm was divided by 730. For the 10 µm wavelength, however, the original heating profile could not be scaled since a 10 µm wavelength has an imaginary index of refraction of 0.1. With such a high index of refraction, all of the irradiant energy is absorbed within microns of the surface. For the 10 µm case, a new heating profile was generated and imported into the non-isothermal flow drop simulations. The temperatures of the varied wavelength cases are shown in Figure 43.

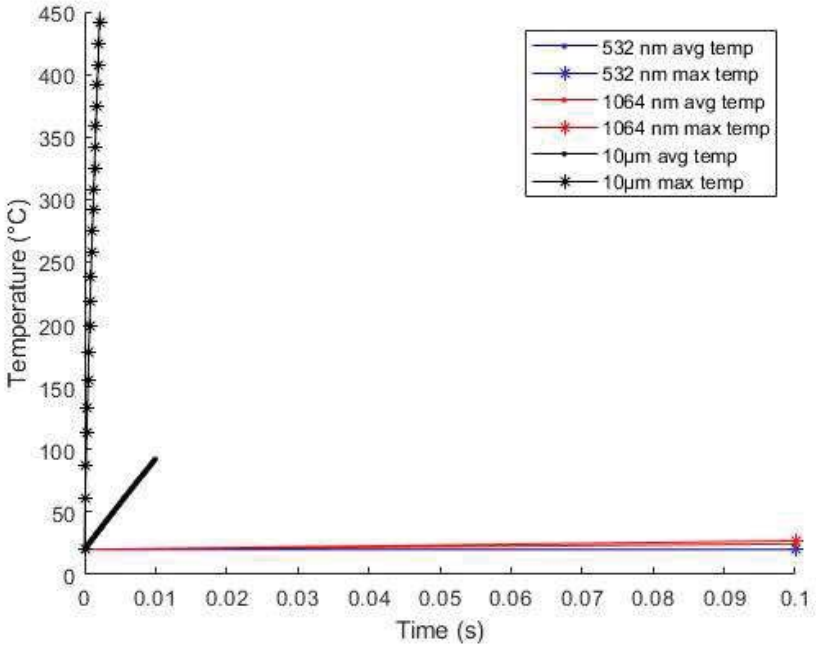


**Figure 43: Max and average temperature for drops irradiated by different wavelengths**

While the 532 and 1064 nm wavelengths do not add significant heat to the drop within the first tenth of a second, the average temperature of the 10 μm drop surpasses the boiling point of water within 10 milliseconds. The 10 μm wavelength certainly pushes drops into the explosive or fast vaporization regime because the energy deposition is great. The average velocity of the drops is shown in Figure 44.

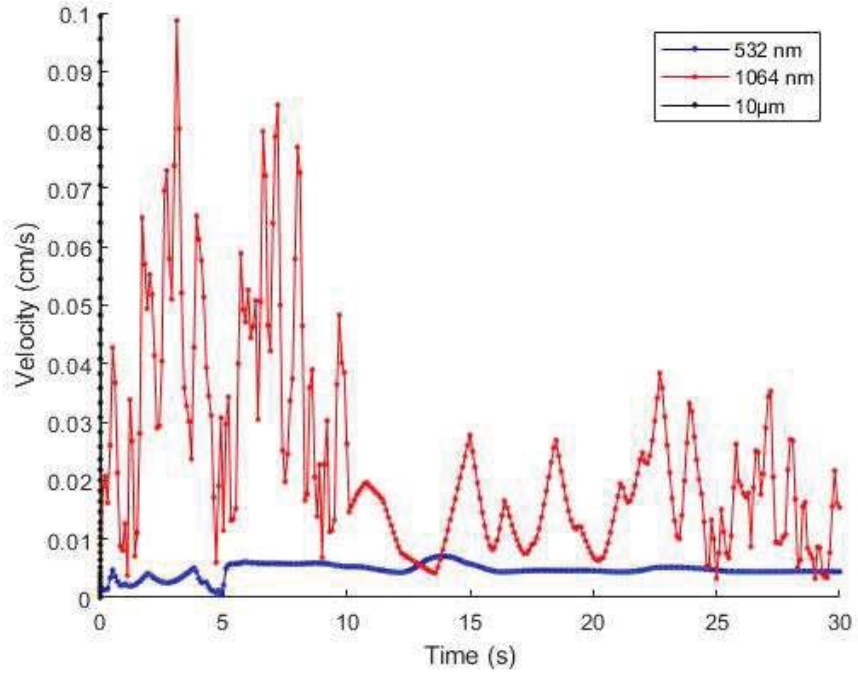

**Figure 44: Volume average velocities for varied irradiant wavelengths**

Because the drop exposed to 10 µm irradiance immediately boiled, it was not simulated beyond 0.1 seconds. The other two irradiant wavelengths were simulated for the full 30 seconds however, and the average velocity of the 1064 nm wavelength is higher than the velocity in the 532 nm drop. The higher absorptivity of 1064 nm generates larger temperature variations which leads to greater buoyancy induced flow.

## Varied Viscosities

To explore the effects of varying viscosity on the internal dynamics of a drop four viscosity relationships were tested. The viscosity of water is a temperature dependent property and COMSOL has a sixth order polynomials to describe viscosity. These polynomials can be edited, and a coefficient magnitude was applied to the entire temperature dependent viscosity to scale the viscosity. Double, half, and sixteen times the viscosity of water were tested. The temperature averages are shown in Figure 45.

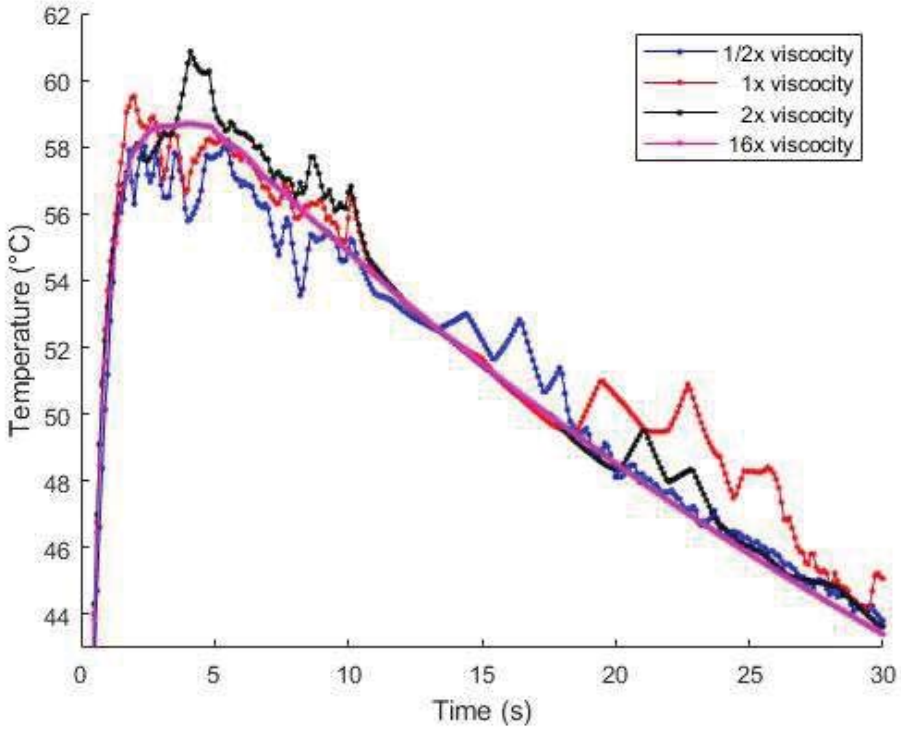


**Figure 45: Volume average temperatures for varied viscosities**

In Figure 45, there is no clear relationship between temperature and the effects of doubling or halving the viscosity of water. The sixteen times viscosity case however seems to indicate that

higher viscosity serves as a dampener to temperature oscillations. Figure 46 shows the effect on velocity.

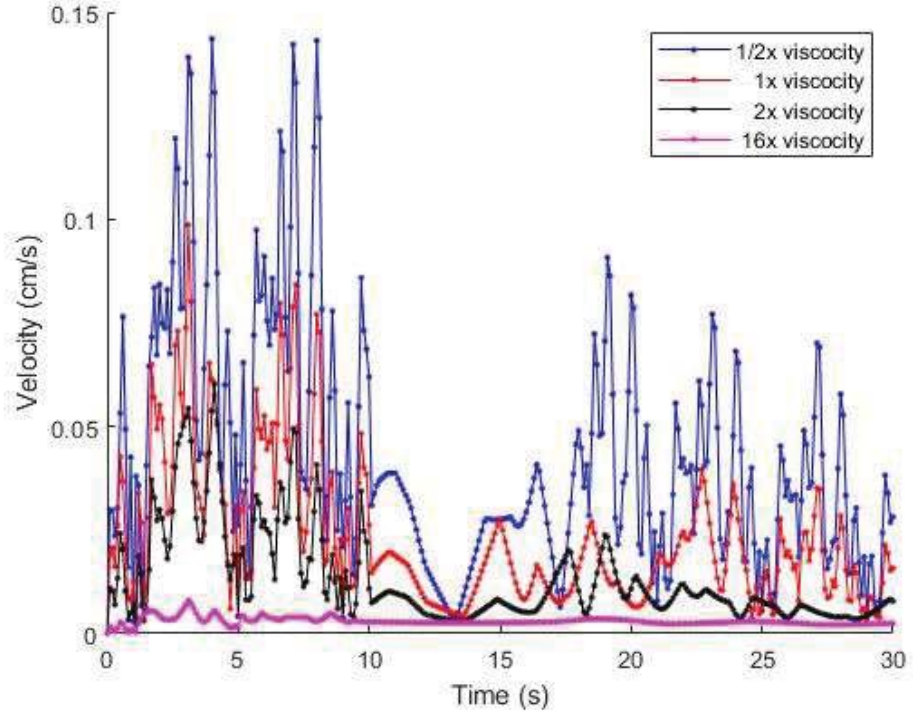


**Figure 46: Volume average velocity for varied viscosities**

In Figure 46, the increased viscosity values have less motion than the lower viscosities. Higher viscosity serves as a dampener for temperature fluctuation, and for internal motion. The elevated viscosity slows the rate at which buoyancy induced forces can bring hot pockets to the surface for convection. Since the heat variation is less prone to motion, the convection at the surface of the drop will vary less dramatically and the oscillations in temperature are greatly reduced, as seen in Figure 45.

# Conclusions

COMSOL Multiphysics is a precise tool used to generated non-isothermal flow data from drop heating simulations. The COMSOL simulations provide precise temperature, velocity, heat deposition, and drop deposition data. This enables analysis of internal drop temperatures and dynamics which cannot be observed experimentally. From including a variety of levels of physics, it is shown that laser heating alone cannot adequately account for the surface temperature variations and motion observed in acoustically levitated drops. Extra forcing is needed to more accurately simulate temperature and velocity dynamics induced by acoustic levitation. One way to add this forcing is by applying an oscillating body force which generates buoyancy induced flow in the x. y, and z directions. Pressure forces incident on a drop that can vary in shape may be more accurate, but allowing the drop shape to vary with pressure forces and surface tension would further complicate the model. Using oblate instead of spherical shapes generates dynamics that are more realistic simply because of the different shape, but with an oblate drop, a normal surface velocity would work poorly because the drop shrinking would cause the drop to become more oblate as it shrank.

From the validation test case, as expected, surface temperatures are consistently lower than volume temperatures. This is due to the convection at the surface of the drop which simulates the effect of evaporation within the drop. While this effect is observed in the simulations, it may not be as prevalent in real laser drop experiments because nucleate can occur internally within the drop which leads to pressure drops around the nucleation sites.

Since smaller droplets have been studied extensively with isothermal assumptions, these simulations dropped that assumption in order to more accurately evaluate buoyancy driven internal dynamics. These dynamics were generated by the non-uniform laser heating profile. When the size of the drops varied, the smaller drops showed lower temperatures and fewer internal dynamics due to the higher surface area to volume ratio which improves heat dissipation, and the reduced length scale which leaves fewer energetic modes available for internal motion. Interestingly however, larger while smaller drops dissipate heat more quickly due to their high surface area to volume ration, larger drops benefit slightly from the internal mixing within them that helps distribute heat to the surface. When the irradiance of the laser varied, higher irradiances generated greater temperatures and greater temperature gradients which induced more motion. At higher irradiances, the vaporization regime changes from slow vaporization to fast, or explosive, vaporization. When the wavelength of the radiation varied, it had similar effects to that of reducing the irradiance by a factor of over 700 when changing the wavelength from 1064 nm to 532 nm. When the wavelength was increased to 10 μm, the absorptivity changed so much that a new heating profile had to be generated using geometrical optics and ray tracing. With an imaginary index of refraction of 0.1, nearly 5 orders of magnitude greater than the imaginary index for 1064 nm, nearly all of the energy was deposited at the surface of the drop where the irradiation was incident. This lead to higher temperatures and temperature gradients for the same irradiance. When the viscosity of the drop varied, increased viscosity was shown to act as both a temperature fluctuation and motion damper within the drop.

Extrapolating these results to HELs, it is likely that through most of the path length of a HEL, drops caught in the beam will be close to the fast vaporization regime. Assuming an aperture of a 30cm diameter, and a power of 100kW, there will only be about 140 $W/cm^2$ right outside the aperture. These assumptions are based on a proposed power range for the new laser weapon HELIOS which is set to be anywhere from 60 to 150kW. At this heating rate, drops will not see explosive vaporization. As the beam propagates towards a target however, the spot size may focus down to a 5cm or even 3cm diameter. With a 5 cm diameter assuming no attenuation, this area and power will yield about $5kW/cm^2$. If the spot size were to focus even further to a 3 cm diameter, then the irradiance without attenuation would exceed $14kW/cm^2$. Since attenuation is certain, and the spot size will likely not focus to smaller than a 5cm diameter, it will take approximately 0.1 seconds for a 1 mm sized drop to reach the boiling point. Since a typical free fall velocity for a drop is on the order of 1 to 10 m/s, the time within the 5 mm spot size would be between 0.05 and 0.005 seconds. This is less time than is needed to reach the boiling point, so free falling rain will likely not vaporize as it passes through the laser. If raindrops are caught in updrafts or if the laser is tracking a target, then the drop exposure may easily exceed 0.1 seconds in which case the drops would be vaporizing. Fog also stays stationary, but due to the high surface area to volume ratio, it is possible that the fog would not heat up enough to vaporize in a second of exposure at 5 $kW/cm^2$. More testing is needed to determine this. If however, a wavelength of 10 μm is utilized, it is likely that any drop that sees greater than 500 $W/cm^2$ will instantaneously vaporize. Since these conclusions are derived from simulations that only account for laser heating and drop dynamics, they are not complete. In order to generate more complete simulations, the surrounding air must also be considered as well as other physical parameters such as heating of the air and shape fluctuations which vary the focusing of the laser rays within the drop.

# References


1. Melfi, S. H., Lawrence, J. D., & McCormick, M. P. (1969). Observation of Raman Scattering by Water Vapor in the Atmosphere. *Applied Physics Letters, 15*(6), 295-297.
2. Werle, P., Miicke, R., & Slemr, F. (1993). The Limits of Signal Averingin in Atmospheric Trace-Gas Monitoring by Tunable Diode-Laser Absorption Spectroscopy (TDLAS). *Applied Physics, B*(57), 131-139.
3. Bradley, L. C., & Herrmann, J. (1974). Phase Compensation for Thermal Blooming. *Applied Optics, 13*(2), 331-334.
4. Smith, D. C. (1977). High-Power Laser Propagation: Thermal Blooming. *Proceedings of the IEEE, 65*(12), 1679-1714.
5. Berk, A., Berstein, L. S., Anderson, G. P., Acharya, P. K., Robertson, D. C., Chetwynd, J. H., & Adler-Golden, S. M. (1998). MODTRAN Cloud and Multiple Scattering Upgrades with Applicaiton to AVIRIS. *Remote Sensing of Environement, 65*, 367-375.
6. Park, B.-S., & Armstrong, R. L. (1989). Laser droplet heating: fast and slow heating regimes. *Applied Optics, 28*(17), 3671-3680.
7. Davies, S. C., & Brock, J. R. (1987). Laser evaporation of droplets. *Applied Optics*, 786-792.
8. C.R. Nave, Evaporation vs Boiling. *Hyperphysics*. Retrieved from: http://hyperphysics.phy-astr.gsu.edu/hbase/hframe.html
9. Tracey, T. E., & Brownell, C. J. (2018). Evaporation and Beam Profile Measurements on an Irradiated Water Drop. Forthcoming in *Journal of Directed Energy*.
10. Brownell, C. J., Tracey, T. E., & Payne, N. (2017). Imaging of Large Water Drops During Laser Heating and Vaporization. OSA Imaging and Applied Optics Congress
11. Sprangle, P., Penano, J., & Hafizi, B. (2005). *Optimum Wavelength and Power for Efficient Laser Propagation in Various Atmospheric Environments.* Washington: Naval Research Laboratory.
12. Armstrong, R. L., O'Rourke, P. J., & Zardecki, A. (1986). Vaporization of irradiated droplets. *Physics of Fluids*, 3573-3581.
13. Tseng, C. C., & Viskanta, R. (2006). Enhancement of water droplet evaporation by radiation absorption. *Fire Safety Journal*, 236-247.
14. Abramzon, B., & Sazhin, S. (2005). Droplet vaporization model in the presence of thermal radiation. *International Journal of Heat and Mass Transfer*, 1868-1873.
15. Pendleton, J. D. (1985). Water droplets irradiated by a pulsed CO2 laser: comparison of computed temperature contours with explosive vaporization patterns. *Applied Optics*, 1631-1637.

16. Chorin, A. J., & Marsden, J. E. (1998). *A Mathematical Introduction to Fluid Mechanics.* Ann Arbor: Edwards Brothers, Inc.

17. Bergman, T. L., Lavine, A. S., Incropera, F. P., & Dewitt, D. P. (2011). *Introduction to Heat Transfer.* Hoboken: John Wiley & Sons, Inc.

18. Doering, C. R., & Gibbon, J. D. (1995). *Applied Analysis of the Navier-Stokes Equations.* New York: Cambridge University Press.

19. Munson, B. R., Okiishi, T. H., Huebsch, W. W., & Rothmayer, A. P. (2013). *Fundamentals of Fluid Mechanics.* Jefferson City: Wiley.

20. Day, P., Manz, A., & Zhang , Y. (2012). *Microdroplet Technology: Principles and Emerging Applications in Biology and Chemistr.* Springer Science & Business Media.

21. *Refraction of Light*. (2012, April 26). Retrieved from Science Learning Hub: https://www.sciencelearn.org.nz/resources/49-refraction-of-light

22. Swinehart, D. F. (1962). *The Beer-Lambert Law.* University of Oregon Eugene.

23. Frei, W. (2015, April 13). *COMSOL*. Retrieved from Modeling Laser-Material Interactions with the Beer-Lambert Law: https://www.comsol.com/blogs/modeling-laser-material-interactions-with-the-beer-lambert-law/

24. Gomez-Perez, N., Rodriguez, J. F., & McWilliams, R. S. (2017). Finite element modeling of melting and fluid flow in the laser-heated diamond-anvil cell. *Journal of Applied Physics*.

25. Pope, S. B. (2000). *Turbulent Flows.* Cambridge University Press.

26. Paul, E. L., Atiemo-Obeng, V. A., & Kresta, S. M. (2004). *Handbook of Industrial Mixing: Science and Practice.* Wiley. Retrieved from http://nomish.yolasite.com/resources/Handbook%20of%20industrial%20mixing%20-%20science%20and%20practice.pdf

27. Felippa, C. A. (2004). *Intoroduction to Finite Element Methods.* Boulder: Department of Aerospace Engineering Sciences.

28. COMSOL. (n.d.). *Free Convection in a Water Glass.* Retrieved from COMSOL: https://www.comsol.com/model/download/469861/models.heat.cold_water_glass.pdf

29. Engineering Toolbox. (2003). *Water – Thermophysical Properties*. Retrieved from: https://www.engineeringtoolbox.com/water-thermal-properties-d_162.html

30. Go, D. (n.d). *Free Convection: Overview*. Retrieved from Notre Dame: https://www3.nd.edu/~sst/teaching/AME60634/lectures/AME60634_F13_lecture25.pdf

31. COMSOL. (n.d). *Luneburg Lens*. Retrieved from COMSOL: https://www.comsol.com/model/luneburg-lens-18455

32. COMSOL. (n.d). *Modeling Laser Beam Absorption in Silica Glass with Beer-Lambert Law*. Retrieved from COMSOL: https://www.comsol.com/model/modeling-laser-beam-absorption-in-silica-glass-with-beer-lambert-law-56101

33. COMSOL. (n.d.). *Evaporative Cooling of Water*. Retrieved from: https://www.comsol.com/model/download/326531/models.heat.evaporative_cooling.pdf

34. COMSOL. (n.d.). *Understanding Stabilization Methods*. Retrieved from: https://www.comsol.com/blogs/understanding-stabilization-methods/

# Appendices

## Appendix A: Free Convection in a Water Glass COMSOL Tutorial

[28] This tutorial shows how to set material domains, set initial conditions, define boundary conditions, define simulation domains, define governing physics, and couple relevant physics in a two-dimensional axisymmetric model. In this simulation, silica glass and water were defined as materials and the entire water cup started at a temperature of 0°C. The ambient temperature was 25°C, and the bottom of the cup had a boundary condition set to the ambient temperature. The physics interfaces coupled in this simulation were laminar flow and heat transfer in fluids; both are part of the CFD Module. The multiphysics coupling between these two in COMSOL is Non-Isothermal Flow (NITF). Results from this simulation are shown in Figure 47.

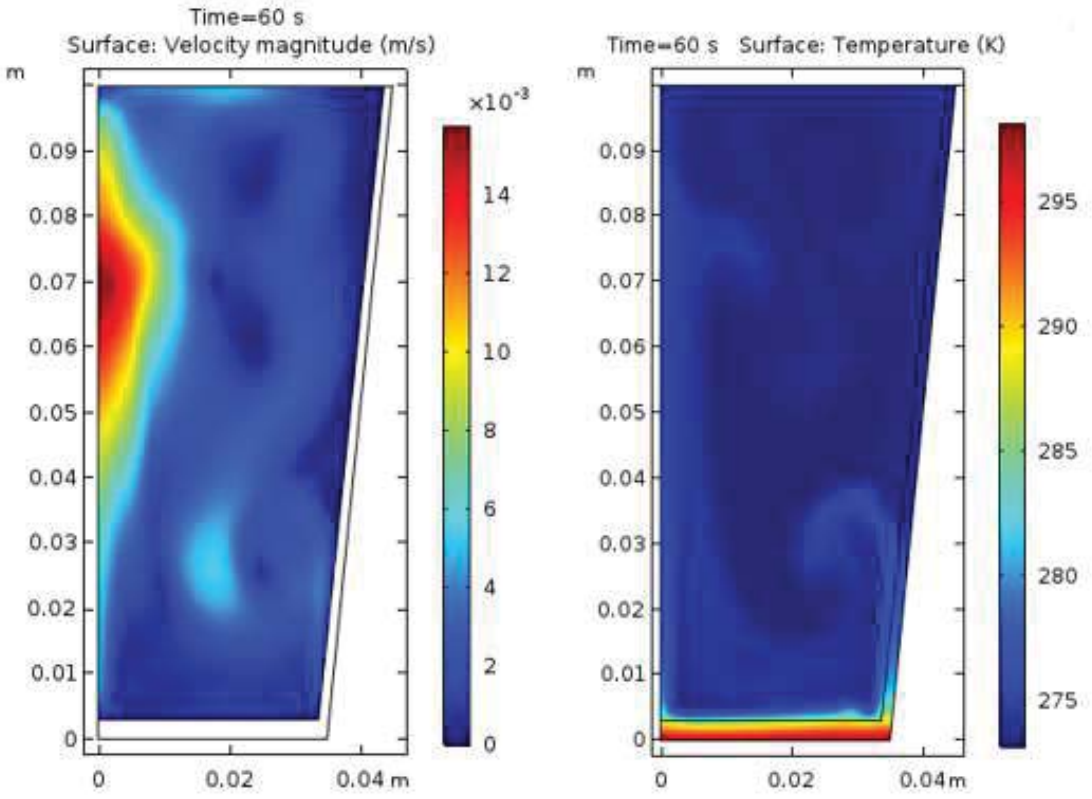


**Figure 47: Free convection in water glass**

This simulation converged in sixteen minutes and shows natural convection within a large domain for a simulation time of two minutes. Knowledge of this simulation served as a basis for all NITF simulations in this research.

## Appendix B: Luneburg Lens COMSOL Tutorial

[31] This tutorial shows how to use Geometrical Optics, define ray release points, constrain ray path lengths, modify material properties, and view intensity data from the simulation. In this Lens tutorial, rays are released from a line incident on the centerline of a sphere with a radially varying index of refraction. The rays are refracted through the sphere and their paths bend according to the changing refractive index. In Figure 48, the variable index of refraction is plotted according to the color bar, and the ray color corresponds to distance from ray origin

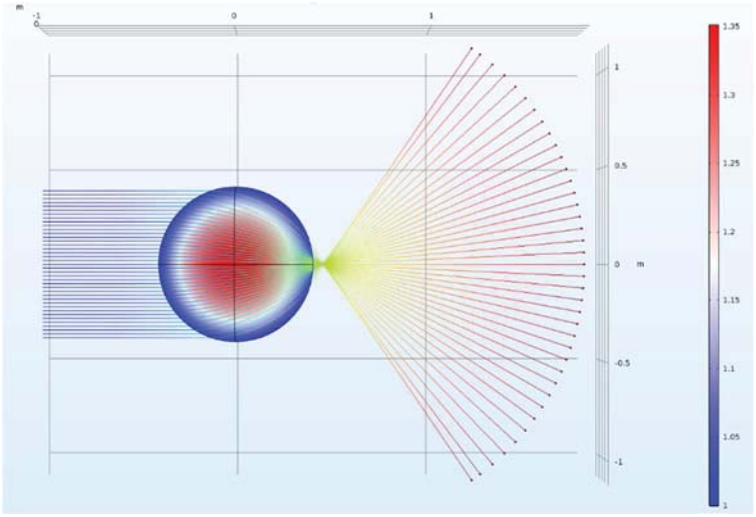

**Figure 48: Laser refraction through Luneburg lens with radially variable refractive index**

This tutorial teaches how to run Ray Tracing module simulations and it shows efficient solver configurations. It also shows how to plot results and extract intensity data.

## Appendix C: Modeling Laser Beam Absorption in Silica Glass with Beer-Lambert Law COMSOL Tutorial

[32] This tutorial models laser attenuation as it passes through silica glass. It utilizes Heat Transfer in Solids, and the Radiative Beam in Absorbing Media interfaces. A temperature dependent absorptivity was defined and the beam intensity incident on the Surface was defined. The results of the simulation are shown in Figure 49.

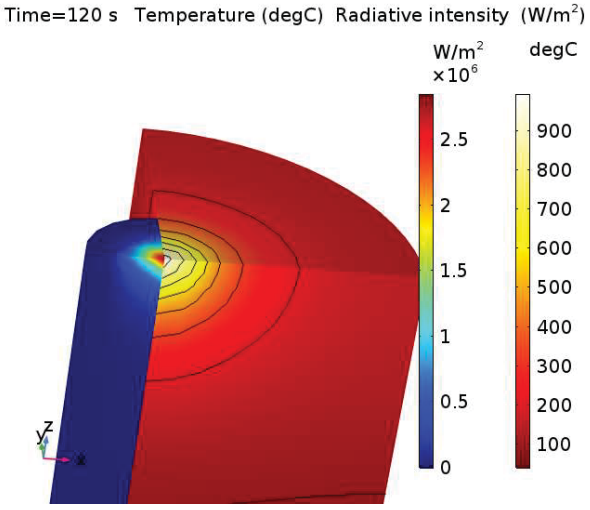


**Figure 49: Temperature and Laser Intensity after 120s of Simulation**

Fruitless attempts were made to conduct this simulation with a liquid, but there is no COMSOL interface between liquids and laser heating. The simulation was modified to include a heat function throughout the glass. This heat source was then modified to simulate a medium with a higher and lower absorptivity. The temperature and heat source profile that model higher and lower absorptivity are shown in Figure 50.

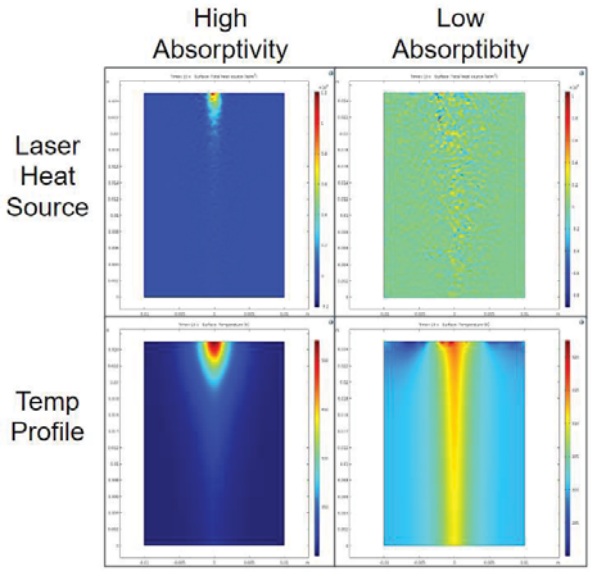


**Figure 50: Heat source (W/m$^3$) and temperature profile for silica glass**

While this heat source does not incorporate absorptivity, this technique of applying defined heating functions to the interior of a domain was used in this study when simulating irradiated drops.

## Appendix D: Evaporative Cooling of Water COMSOL Tutorial

[33] Moisture considerations link the mass flux with the evaporative cooling of the drop. Warmer air can hold more water vapor, so the effects of evaporative cooling will be greater at warmer water temperatures.

Including moisture transport and evaporative cooling complicates drop simulations even further because it will requires the simulation of the surrounding air to track the moisture and temperature around the drop. This will make the simulation more realistic since the cooling effect of evaporation significantly contributes to the heat loss.

In this tutorial, air at an ambient temperature of 20°C flows around a cup at 80°C. The interfaces used were Turbulent Flow, Heat Transfer in Moist Air, and Moisture Transport in Air. The Turbulent Flow and Heat Transfer in Moist Air only consider the air flowing around the cup. The moisture enters the air with the Moisture Transport in Air interface through a defined "Wet Surface". Three multiphysics couplings were used, including Heat and Moisture, which couples Heat Transfer in Moist Air and Moisture Transport in Air, NITF, which couples Heat Transfer in Moist Air and Turbulent Flow, and Moisture Flow, which couples Heat Transfer in Moist Air and Moisture Transport in Air. The relative humidity in the air flowing over the cup is shown in Figure 51.

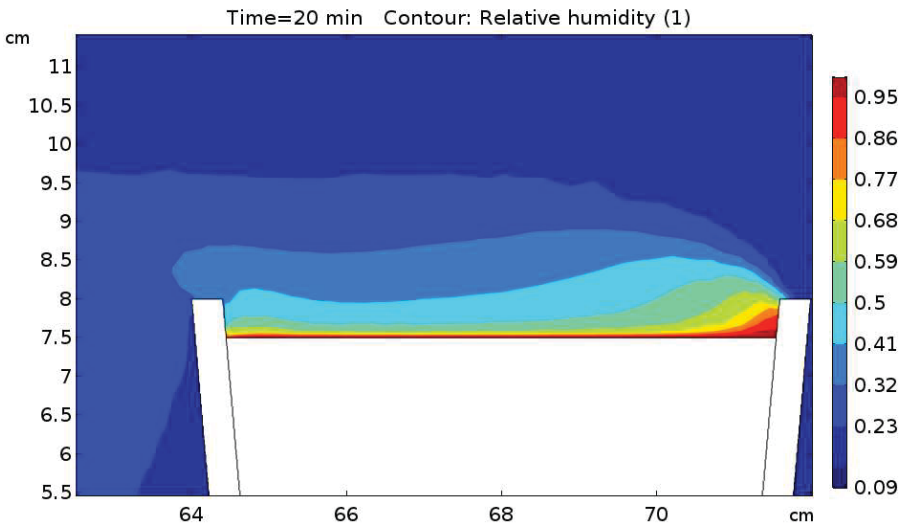


**Figure 51: Relative Humidity of Air Flowing Over Warm Water Cup**

Two separate studies were conducted: one with evaporative cooling effects included, and one with only conduction effects included. In both of these studies, the average water temperature was calculated at each time step, and the results are shown in Figure 35.

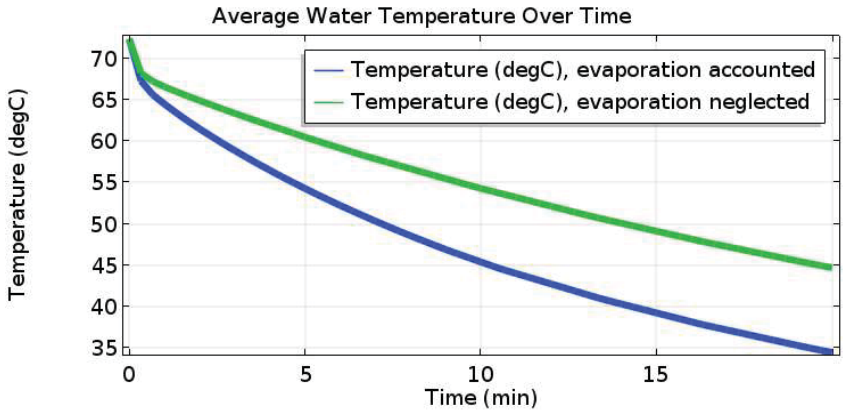


**Figure 52: Average Water Temperature With and Without Evaporative Cooling Effects**

In Figure 52, the difference in cooling rates between the two scenarios is greater at warmer temperatures than at cooler ones. This difference makes moisture tracking essential for simulations that are more realistic.

## Appendix E: MATLAB ray tracing intensity contour

Plot Rays through sphere

```
clear; close all; clc;

% number of rays
y_min=0; %lowest ray (mm)
y_step=.05; %distance between rays
y_max=5; %highest ray (mm)
% how many points per ray?
num_pts=100; % define a number of points plotted on ray
% number of bins for contour plot
bin_number=100;

figure(1)
hold on
xlim([-6 6]); % set x and y axis bounds
ylim([-6 6]);
r=5; % radius in (mm)
x1=linspace(-r,r);   % generate x values to plot circle
y1=sqrt(r^2-(x1.^2));  % calc y from x
y2=-sqrt(r^2-(x1.^2));  % negative y values
p1=plot(x1,y1);p1.Color='b';p1.LineWidth=2; %plot circle top
p2=plot(x1,y2);p2.Color='b';p2.LineWidth=2; % plot circle bottom
p3=refline(0,0);p3.Color='r';p3.LineWidth=.5; %horizontal line through (0,0)

title('Plot of intensity')
xlabel('X axis (mm)')
ylabel('Y axis (mm)')


y=y_min:y_step:y_max;  %incident ray locaCtions
num_rays=length(y);
x=(r^2-y.^2).^(1/2); %x intercept of rays
scatter(-x,y,'*');   %scatter intercepts
m=x./(r^2-x.^2).^(.5);%calculate the slope at each intercept
n=-1./m;             %calculate normal slope

for i=1:length(n)
p=refline(n(i),0);p.LineWidth=2;  %plot normal lines to each ray intersect
end
ang=atan(abs(n)); % gives normal slope in radians

y_vert=get(gca,'ylim'); % used to plot vertical line
hold on
p4=plot([-r -r],y_vert);p4.Color='k';p4.LineWidth=.5;  %plot two vertical lines
p5=plot([-2*r -2*r],y_vert);p4.Color='k';p4.LineWidth=.5;
pbaspect([1 1 1]) %scaling of figure

for i=1:length(n)
    hline=refline(0,y(i)); % plot the incident rays
    hline.LineWidth=2;hline.Color='g';
```

```
end

%apply Snell idx_1*sin(theta_1)=idx_2*sin(theta_2)
index=1.333; %index of refraction
new_ang=asin(sin(ang)/index); % calculate theta_2
RayAng=ang-new_ang; %angle of new slope in rads
rayN=-atan(ang-new_ang); %new slope of ray in drop

for i=1:length(x) %plot new ray slopes
    hline=refline(rayN(i),rayN(i)*x(i)+y(i));
    hline.Color='r'; hline.LineWidth=2;
end
xlim([-6 6]); %resize figure
ylim([-6 6]);
```

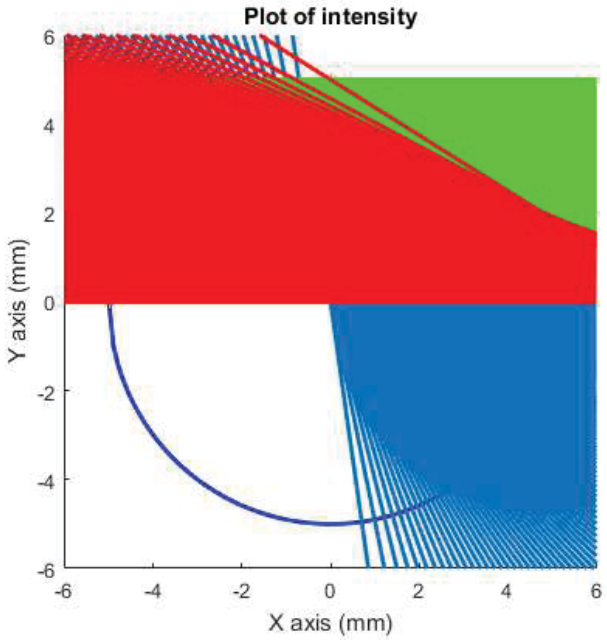


next figure

```
figure(2) % plot top half of circle
p1=plot(x1,y1);p1.Color='b';p1.LineWidth=.5;
hold on
xlim([-7 5]); %size figure
ylim([0 6]);
pbaspect([2 1 1]); %set aspect ratio
for i=1:length(x) % plot rays entering drop
    hline=refline(rayN(i),rayN(i)*x(i)+y(i));
    hline.Color='r';
end
scatter(-x,y,'*'); %plot ray intersections
xlim([-7 5]); % size figure
ylim([0 6]);
```

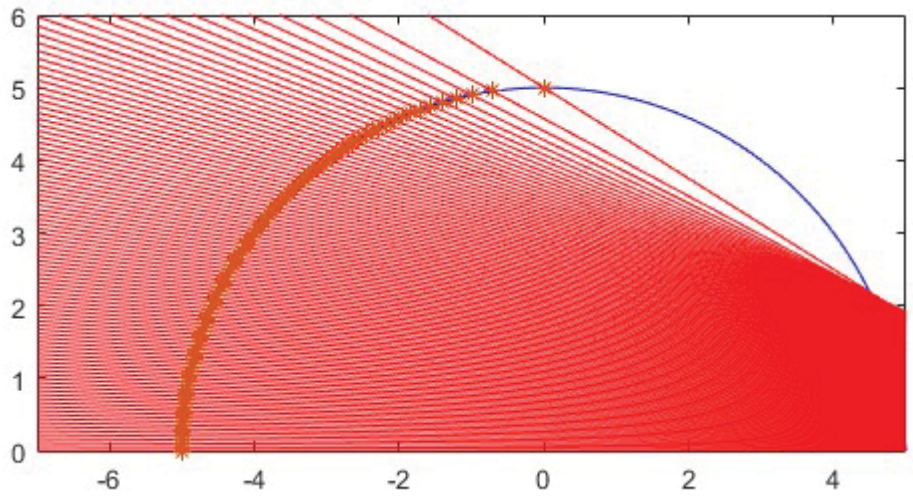


Bins fig

```
figure(3) % plot top half of circle
p1=plot(x1,y1);p1.Color='b';p1.LineWidth=.5;
hold on
xlim([-7 5]); %size figure
ylim([0 6]);
pbaspect([2 1 1]); %set aspect ratio
for i=1:length(x) % plot rays entering drop
    hline=refline(rayN(i),rayN(i)*x(i)+y(i));
    hline.Color='r';
end
scatter(-x,y,'*'); %plot ray intersections
xlim([-7 5]); % size figure
ylim([0 6]);

%num_pts=10 % define a max number of points per ray
step=2*r/num_pts; %delta step

% determine points along each ray at step interval
for j=1:num_rays
    for i=2:num_pts+1
        x(i,j)=x(i-1,j)-step.*cos(RayAng(j));
        y(i,j)=y(i-1,j)-step.*sin(RayAng(j));
    end
end

%plot points along rays
for i=1:num_rays
scatter(-x(:,i),y(:,i))
end
```

make the contour plot!!!

```
%  bin_number=100; Defined at top
Xedges = linspace(-1.1*r,1.1*r,bin_number+1);
Yedges = linspace(-1.1*r,1.1*r,bin_number+1);
N = histcounts2(x,y,Xedges,Yedges);
X_plot=repmat(Xedges(1:bin_number),bin_number,1);
Y_plot=repmat(Yedges(1:bin_number)',1,bin_number);
figure(5)
clf
axis([-5.5 5.4 -.25 5.4])
[C,h] = contourf(X_plot,Y_plot,(((fliplr((N+1)')/1000000))),100);
set(h,'LineColor','none')
hold on
p1=plot(x1,y1);p1.Color='r';p1.LineWidth=2; %plot circle top
%p2=plot(x1,y2);p2.Color='r';p2.LineWidth=2; % plot circle bottom
axis([-5.5 5.4 -.25 5.4])
```

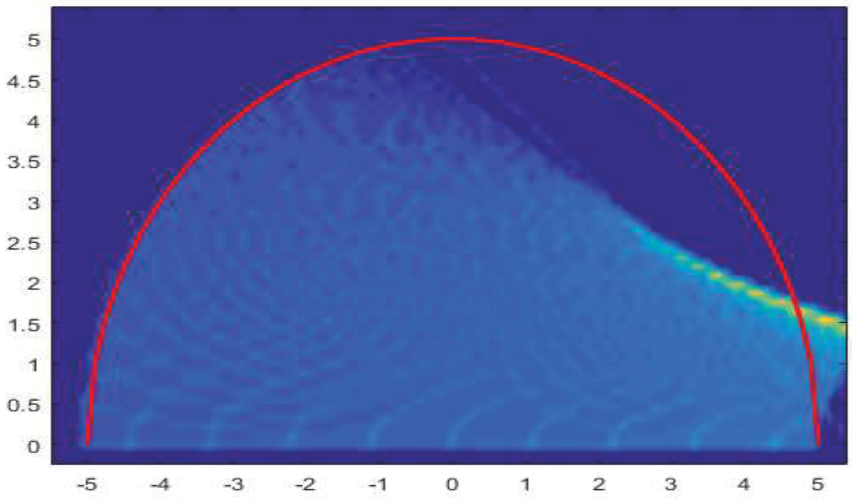


*Published with MATLAB® R2016b*

**Appendix F: COMSOL data tabulation code**

```
model.result().numerical().remove("min3");
model.result().numerical().remove("av3");
model.result().numerical().remove("max3");
model.result().numerical().remove("min4");
model.result().numerical().remove("av4");
model.result().numerical().remove("max4");

model.result().numerical().remove("min5");
model.result().numerical().remove("av5");
model.result().numerical().remove("max5");
model.result().numerical().remove("min6");
model.result().numerical().remove("av6");
model.result().numerical().remove("max6");

model.result().numerical().remove("min7");
model.result().numerical().remove("av7");
model.result().numerical().remove("max7");
model.result().numerical().remove("min8");
model.result().numerical().remove("av8");
model.result().numerical().remove("max8");

model.result().numerical().create("min3", "MinSurface");
model.result().numerical().create("av3", "AvSurface");
model.result().numerical().create("max3", "MaxSurface");
model.result().numerical().create("min4", "MinVolume");
model.result().numerical().create("av4", "AvVolume");
model.result().numerical().create("max4", "MaxVolume");

model.result().numerical().create("min5", "MinSurface");
model.result().numerical().create("av5", "AvSurface");
model.result().numerical().create("max5", "MaxSurface");
model.result().numerical().create("min6", "MinVolume");
model.result().numerical().create("av6", "AvVolume");
model.result().numerical().create("max6", "MaxVolume");

model.result().numerical().create("min7", "MinSurface");
model.result().numerical().create("av7", "AvSurface");
model.result().numerical().create("max7", "MaxSurface");
model.result().numerical().create("min8", "MinVolume");
model.result().numerical().create("av8", "AvVolume");
model.result().numerical().create("max8", "MaxVolume");

with(model.result().numerical("min3"));
  setIndex("expr", "T", 0);
```

```
  setIndex("unit", "degC", 0);
endwith();
with(model.result().numerical("av3"));
  setIndex("expr", "T", 0);
  setIndex("unit", "degC", 0);
endwith();
with(model.result().numerical("max3"));
  setIndex("expr", "T", 0);
  setIndex("unit", "degC", 0);
endwith();
with(model.result().numerical("min4"));
  setIndex("expr", "T", 0);
  setIndex("unit", "degC", 0);
endwith();
with(model.result().numerical("av4"));
  setIndex("expr", "T", 0);
  setIndex("unit", "degC", 0);
endwith();
with(model.result().numerical("max4"));
  setIndex("expr", "T", 0);
  setIndex("unit", "degC", 0);
endwith();

with(model.result().numerical("min5"));
  setIndex("expr", "spf.U", 0);
  setIndex("unit", "cm/s", 0);
endwith();
with(model.result().numerical("av5"));
  setIndex("expr", "spf.U", 0);
  setIndex("unit", "cm/s", 0);
endwith();
with(model.result().numerical("max5"));
  setIndex("expr", "spf.U", 0);
  setIndex("unit", "cm/s", 0);
endwith();
with(model.result().numerical("min6"));
  setIndex("expr", "spf.U", 0);
  setIndex("unit", "cm/s", 0);
endwith();
with(model.result().numerical("av6"));
  setIndex("expr", "spf.U", 0);
  setIndex("unit", "cm/s", 0);
endwith();
with(model.result().numerical("max6"));
  setIndex("expr", "spf.U", 0);
  setIndex("unit", "cm/s", 0);
```

```
endwith();

with(model.result().numerical("min7"));
  setIndex("expr", "spf.vort_magn", 0);
endwith();
with(model.result().numerical("av7"));
  setIndex("expr", "spf.vort_magn", 0);
endwith();
with(model.result().numerical("max7"));
  setIndex("expr", "spf.vort_magn", 0);
endwith();
with(model.result().numerical("min8"));
  setIndex("expr", "spf.vort_magn", 0);
endwith();
with(model.result().numerical("av8"));
  setIndex("expr", "spf.vort_magn", 0);
endwith();
with(model.result().numerical("max8"));
  setIndex("expr", "spf.vort_magn", 0);
endwith();

model.result().numerical("min3").selection().all();
model.result().numerical("av3").selection().all();
model.result().numerical("max3").selection().all();

model.result().numerical("min4").selection().all();
model.result().numerical("av4").selection().all();
model.result().numerical("max4").selection().all();

model.result().numerical("min5").selection().all();
model.result().numerical("av5").selection().all();
model.result().numerical("max5").selection().all();

model.result().numerical("min6").selection().all();
model.result().numerical("av6").selection().all();
model.result().numerical("max6").selection().all();

model.result().numerical("min7").selection().all();
model.result().numerical("av7").selection().all();
model.result().numerical("max7").selection().all();

model.result().numerical("min8").selection().all();
model.result().numerical("av8").selection().all();
model.result().numerical("max8").selection().all();
```

```
with(model.result().numerical("min3"));
  set("table", "tbl9");
endwith();
model.result().numerical("min3").setResult();
with(model.result().numerical("av3"));
  set("table", "tbl9");
endwith();
model.result().numerical("av3").appendResult();
with(model.result().numerical("max3"));
  set("table", "tbl9");
endwith();
model.result().numerical("max3").appendResult();

with(model.result().numerical("min4"));
  set("table", "tbl9");
endwith();
model.result().numerical("min4").appendResult();
with(model.result().numerical("av4"));
  set("table", "tbl9");
endwith();
model.result().numerical("av4").appendResult();
with(model.result().numerical("max4"));
  set("table", "tbl9");
endwith();
model.result().numerical("max4").appendResult();

with(model.result().numerical("min5"));
  set("table", "tbl9");
endwith();
model.result().numerical("min5").appendResult();
with(model.result().numerical("av5"));
  set("table", "tbl9");
endwith();
model.result().numerical("av5").appendResult();
with(model.result().numerical("max5"));
  set("table", "tbl9");
endwith();
model.result().numerical("max5").appendResult();
with(model.result().numerical("min6"));
  set("table", "tbl9");
endwith();
model.result().numerical("min6").appendResult();
with(model.result().numerical("av6"));
  set("table", "tbl9");
endwith();
```

```
model.result().numerical("av6").appendResult();
with(model.result().numerical("max6"));
  set("table", "tbl9");
endwith();
model.result().numerical("max6").appendResult();

with(model.result().numerical("min7"));
  set("table", "tbl9");
endwith();
model.result().numerical("min7").appendResult();
with(model.result().numerical("av7"));
  set("table", "tbl9");
endwith();
model.result().numerical("av7").appendResult();
with(model.result().numerical("max7"));
  set("table", "tbl9");
endwith();
model.result().numerical("max7").appendResult();

with(model.result().numerical("min8"));
  set("table", "tbl9");
endwith();
model.result().numerical("min8").appendResult();
with(model.result().numerical("av8"));
  set("table", "tbl9");
endwith();
model.result().numerical("av8").appendResult();
with(model.result().numerical("max8"));
  set("table", "tbl9");
endwith();
model.result().numerical("max8").appendResult();
```